

© 2019 by Akshat Puri. All rights reserved.

MEASUREMENT OF ANGULAR AND MOMENTUM DISTRIBUTIONS OF CHARGED
PARTICLES WITHIN AND AROUND JETS IN Pb+Pb AND pp COLLISIONS AT
 $\sqrt{S_{NN}} = 5.02$ TeV WITH ATLAS AT THE LHC

BY

AKSHAT PURI

DISSERTATION

Submitted in partial fulfillment of the requirements
for the degree of Doctor of Philosophy in Physics
in the Graduate College of the
University of Illinois at Urbana-Champaign, 2019

Urbana, Illinois

Doctoral Committee:

Professor Matthias Grosse Perdekamp, Chair
Professor Anne Marie Sickles, Advisor
¹ Professor Lance Cooper
Professor Bryce Gadaway

Abstract

2 Heavy ion collision experiments have been centered around studying the extreme state of matter formed in
3 such collisions, the quark-gluon plasma. There have been efforts to measure and characterize this state of
4 matter for almost two decades, first at the Relativistic Heavy Ion Collider and subsequently at the Large
5 Hadron Collider. While there have been different approaches to study it, correlated particle showers called
6 jets have found a special place as a probe of the QGP. Arising from highly energetic collisions between
7 partons, jets are formed early enough in heavy ion collisions that they experience the formation of the QGP
8 and its evolution. They are modified from what they would be in a vacuum, and studying these modifications
9 can give insight into the properties of the QGP as well as the strong interaction.

10 Jet measurements can focus on a variety of observables like yields, momenta, or fragmentation patterns,
11 each with its own limitations and advantages. This thesis presents a measurement of the angular distribution
12 of charged particles around the jet axis as measured by the ATLAS detector for Pb+Pb and pp collisions
13 with a center of mass energy of $\sqrt{s_{NN}} = 5.02$ TeV. Comparing the measurement in the two systems shows
14 that charged particles carrying a transverse momenta p_T of less than 4 GeV have a broader distribution
15 in Pb+Pb collisions, while those with $p_T > 4$ GeV have a narrower distribution. Furthermore, there is an
16 enhancement for particles with $p_T < 4$ GeV in Pb+Pb collisions, with the enhancement increasing up to 2
17 for $r < 0.3$ from the jet axis, and remaining constant for $0.3 < r < 0.6$. Charged particles with $p_T > 4$ GeV
18 show a small enhancement in the jet core for $r < 0.05$, and are increasingly suppressed up to 0.5 for $r < 0.3$.
19 This depletion remains constant for $0.3 < r < 0.6$.

For my Mother, Father, and Brother

Contents

22	Chapter 1 Introduction	1
24	1.1 Quantum Chromodynamics	1
25	1.2 Quark-Gluon Plasma	4
26	1.3 Heavy Ion Collisions	8
27	1.4 Jets and Jet Quenching	12
28	1.4.1 Jets in e^+e^- collisions	12
29	1.4.2 Jets in pp collisions	13
30	1.4.3 Jets in heavy ion collisions	16
31	1.4.4 Jet Algorithms	18
32	Chapter 2 Major Jet Measurements	21
33	2.1 Hadron Supresion	21
34	2.2 Dijet Balance: x_J	22
35	2.3 Modification of jet yields: R_{AA}	23
36	2.4 Jet Fragmentation	25
37	2.5 Jet Profile	27
38	Chapter 3 Jet Energy Loss Models	30
39	3.1 Effective Quenching	30
40	3.2 Jet Fluid model	33
41	3.3 Hybrid Model	36
42	Chapter 4 LHC and the ATLAS Detector	41
43	4.1 The Large Hadron Collider	41
44	4.2 The ATLAS Detector	43
45	4.2.1 Inner Detector	43
46	4.2.2 Calorimeter	45

47	4.2.3 Muon Spectrometer	46
48	4.2.4 Other subsystems	47
49	4.3 Jet Reconstruction for Heavy Ion Collisions in ATLAS	48

Chapter 1

Introduction

50 This section shall discuss the theoretical background necessary to understand jet measurements. It will
51 discuss the fundamentals of quantum chromodynamics (QCD), the quark gluon plasma and the heavy ion
52 collision system it is formed in, and finally jets and jet energy loss.

53 1.1 Quantum Chromodynamics

54 Quantum Chromodynamics is a gauge theory with SU(3) symmetry that describes the dynamics of the strong
55 interactions between quarks and gluons. It is part of the Standard Model [1], the building blocks of which
56 are shown in Figure 1.1.

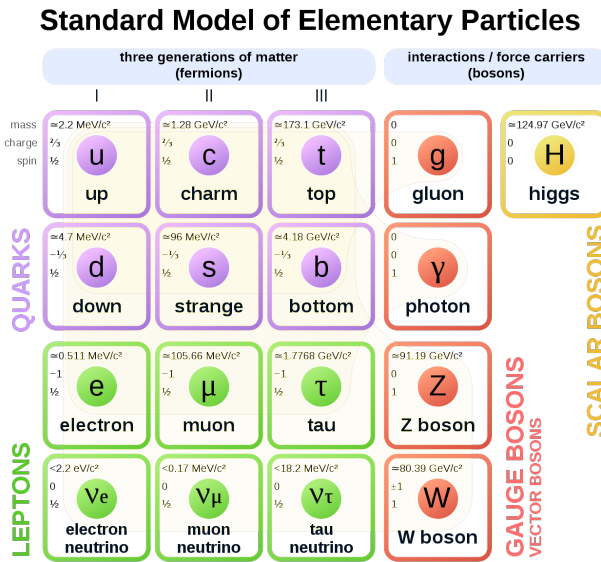


Figure 1.1: The elementary particles of the standard model. Figure taken from Ref. [2].

57 Quarks are fermions with a spin of $1/2$, and carry a fractional electric charge as well as a color charge.
58 They all have mass and come in six flavors: up, down, strange, charm, top, bottom. The lightest quarks

59 (u and d) combine and form stable particles, while the heavier quarks can only be produced in energetic
 60 environments and decay rapidly. Gluons are gauge bosons (force carriers) with a spin of 1, and are what hold
 61 quarks together. The dynamics of the quarks and gluons, collectively referred to as partons are described by
 62 the QCD Lagrangian given by [3]:

$$\mathcal{L}_{\text{QCD}} = \sum_q \bar{\psi}_{q,a} (i\gamma^\mu \partial_\mu \delta_{ab} - g_s \gamma^\mu t_{ab}^C \mathcal{A}_\mu^C - m_q \delta_{ab}) \psi_{q,b} - \frac{1}{4} F_{\mu\nu}^A F^{A\mu\nu} \quad (1.1)$$

63 where $\psi_{q,a}$ and $\psi_{q,b}$ are quark-field spinors for a quarks with flavor q , mass m_q , and color a and b respectively,
 64 with the values for a and b ranging from 1 to 3 (for the three colors). The \mathcal{A}_μ^C corresponds to the gluon field
 65 with C taking values from 1 through 8 (for the 8 types of gluons). The t_{ab}^C corresponds to the Gell-Mann
 66 matrices that are the generators of the SU(3) group, and dictate the rotation of the quarks color in SU(3)
 67 space when it interacts with a gluon. The coupling constant is encoded within g_s , which is defined by
 68 $g_s \equiv \sqrt{4\pi\alpha_s}$. The field tensor $F_{\mu\nu}^A$ can be written in terms of the structure constants of the SU(3) group
 69 f_{ABC} , and is given by:

$$F_{\mu\nu}^A = \partial_\mu \mathcal{A}_\nu^A - \partial_\nu \mathcal{A}_\mu^A - g_s f_{ABC} \mathcal{A}^B \mathcal{A}^C \quad (1.2)$$

70 While many parallels can be drawn between Quantum Electrodynamics (QED, the theory that describes
 71 photons and electrons) and QCD, the main difference between the two comes from the gluon-gluon interactions
 72 allowed in QCD, making it non-Abelian. These interactions can be summarized as shown in Figure 1.2.

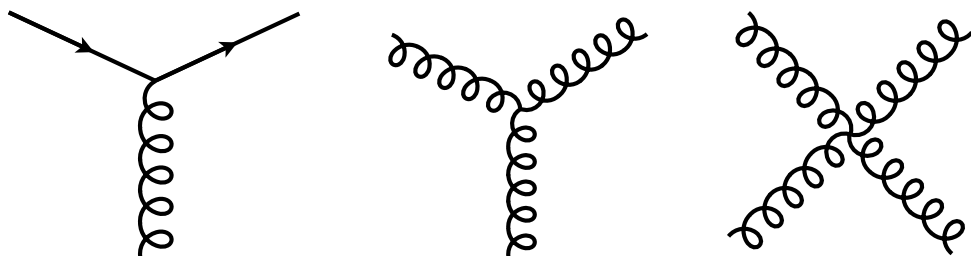


Figure 1.2: The allowed vertices in QCD. The vertices involving two or more gluons are unique to QCD and do not have a QED analog.

73 A core feature of QCD is that the coupling constant α_s has an energy dependence shown in Figure 1.3.
 74 This dependence can be expressed in terms of the β function as

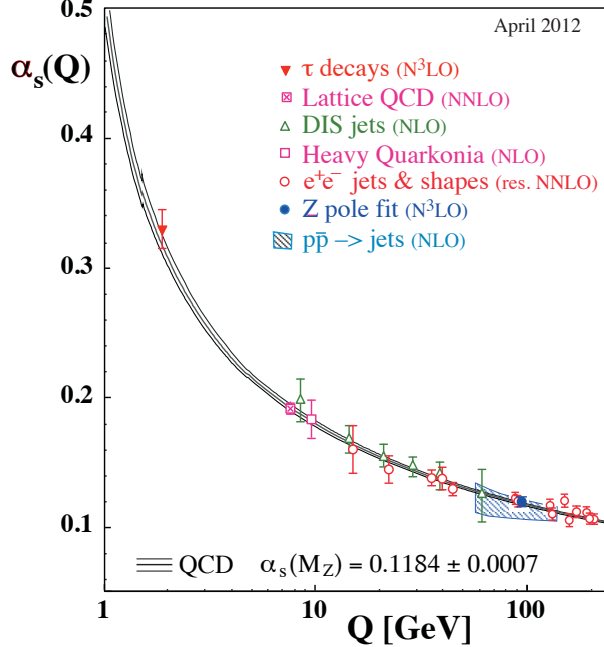


Figure 1.3: The running coupling constant α_s as a function of the momentum transfer Q . Figure taken from Ref. [3].

$$Q^2 \frac{\partial \alpha_s(Q^2)}{\partial Q^2} = \beta(\alpha_s(Q^2)) \quad (1.3)$$

where Q is the momentum transfer in the particle reaction ¹. The beta function can be expressed using perturbative QCD (pQCD) as:

$$\beta(\alpha_s) = -(b_0 \alpha_s^2 + b_1 \alpha_s^3 + b_2 \alpha_s^4 \dots) \quad (1.4)$$

where the coefficients b_i depend on the number of colors and flavors. This running coupling constant is small and asymptotically tends to zero at large energy scales (or at small distances) and is large at small energy scales (large distances). This running coupling phenomenon leads to two key behaviors: asymptotic freedom and color confinement.

Asymptotic Freedom: At high energy scales (small distances), the QCD coupling constant α_s is small and tends to zero, implying a free particle behavior of quarks and gluons[4, 5]. This has been observed

¹The momentum transfer Q is the amount of momentum transferred in a scattering process.

83 by a variety of deep inelastic scattering (DIS) experiments [6–19]. These scattering experiments shown
 84 in Figure 1.4, probe the interior of a nucleon using highly energetic leptons like electrons. The electron
 85 scatters off of the target proton, producing a lepton and a hadron shower. First done by MIT-SLAC [20, 21],
 86 these DIS experiments showed the weak Q^2 dependence on the inelastic scattering cross-sections, as well as
 87 Bjorken scaling [22], where the proton structure functions are independent of the momentum transfer. These
 88 experiments revealed the point-like constituents of the proton and paved the road to an asymptotically free
 89 theory.

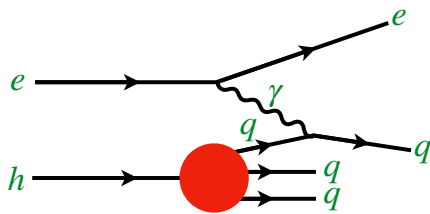


Figure 1.4: Schematic of the deep inelastic scattering experiment.

90 **Color Confinement** The opposite end of the running coupling constant phenomenon is color confinement.
 91 Proved to be a consequence of asymptotic freedom in Ref [23], this property of QCD described in
 92 Ref. [24] forbids the direct observation of free quarks and gluons, allowing only for composite particles that
 93 are color singlets. While have been numerous efforts to understand the source of this phenomenon like in
 94 Refs. [25–31], these are based on numerical calculations. An analytic proof of color confinement still escapes
 95 description and in fact, is one of the Millennium Problems [32].

96 1.2 Quark-Gluon Plasma

97 The quark-gluon plasma is a state of matter that comprises of free partons and is formed in extreme conditions
 98 of temperature and pressure [33]. Its study is motivated by the fact that is the only way to access the
 99 dynamics of partons that are otherwise confined within hadrons. Moreover, its thermodynamic properties are
 100 of particular interest since it filled the early universe a few microseconds after the Big Bang [34]. The QGP
 101 also forms the core of neutron-stars [35] and the recent detection of gravitational waves from a neutron-star
 102 merger [36] has opened new avenues of investigation [37–39]. These studies have the potential to provide
 103 information into the nuclear equation of state since the dynamics of the merger are sensitive to the behavior
 104 of extremely dense nuclear matter [40]. The increase in temperatures and density during the merger results
 105 in different pre- and post-merger signals of gravitational-waves that suggest a signature of a first-order

hadron-quark phase transition at extreme densities [41]. Colliders like RHIC and the LHC on the other hand probe regions that have comparatively low baryon densities. Lattice QCD calculations in these regions show that the transition between a hadronic gas and the QGP occurs at a temperature of approximately 160 MeV and corresponds to an energy density of 0.5 GeV/fm³ [42]. This is a smooth crossover that spans a 20–30 MeV temperature range, and can be seen in the QCD phase diagram shown in Figure 1.5. This phase diagram shows the transition between free quarks and gluons within the QGP and the confined quarks and gluons within hadrons, as a function of temperature T and baryon chemical potential μ .

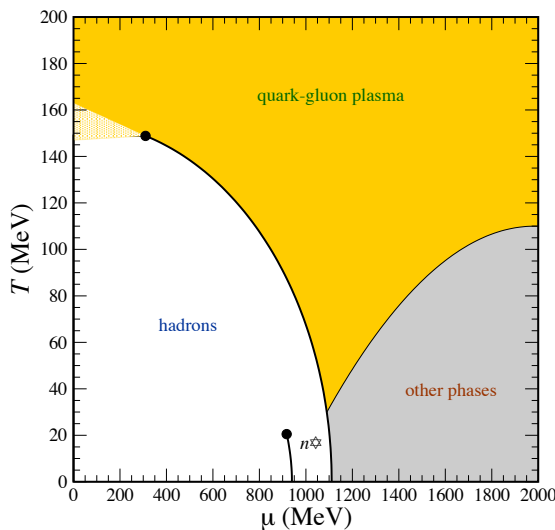


Figure 1.5: The QCD phase diagram of nuclear matter as a function of temperature T and baryon chemical potential μ . The n^* denotes a neutron star. Figure from Ref. [43].

When formed in a heavy ion collision, this state of matter exists for 1–10 fm/c, depending on the collision energy [44]. Thermal photons from the QGP reveal that it reaches temperatures of 300–600 MeV in central collisions at 200 GeV [45] and 2.76 TeV [46], showing very little collision energy dependence. As the QGP cools via expansion, its temperature drops below the critical temperature of QCD phase transitions and it forms a hadron gas. This process, referred to as a chemical freeze-out, occurs at about 160 MeV [47–49]. The hadrons formed in this stage continue to interact with each other, but have energies below the threshold for inelastic particle production, resulting mainly in modifications to their momentum spectra. This continues till the medium cools further and reaches what is called a thermal freeze-out at 100–150 MeV [50–53].

The QGP was initially thought to be a weakly coupled parton gas because of asymptotic freedom from QCD. The highly energetic collisions such as those at the LHC would imply weak interactions between the partons that make up the plasma [34, 54, 55]. This would result in rare scatterings between the constituents of the gas, washing out any spatial anisotropies based on “lumpy”-ness of the colliding nuclei or the collision

geometry. On the other hand, a strong coupling within the QGP would result in the pressure gradients in the medium being driven by hydrodynamics and spatial anisotropies would be transformed to momentum anisotropies in the particles produced as shown in Figure 1.6 [56]. In this picture, the non-uniform structure of the colliding nuclei would cause a momentum anisotropy [57] that would be further enhanced when looking at collisions that are less central and do not have perfect overlap between the colliding nuclei [58, 59]. These observations were seen in azimuthal correlation measurements implying that the medium is indeed strongly coupled [60–63].

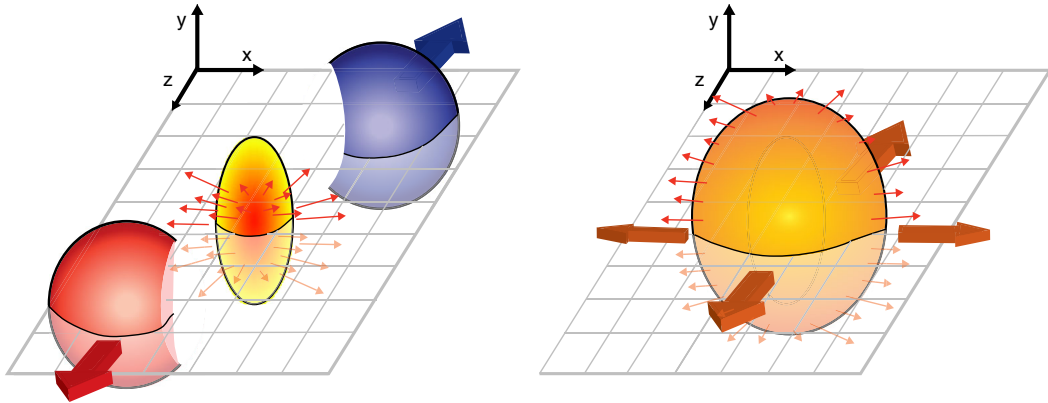


Figure 1.6: Schematic diagrams of the initial overlap region (left) and the final spatial anisotropy generated (right). Taken from [64].

The azimuthal angular distribution of particles produced in a heavy ion collision can be expanded in a Fourier series as [65]:

$$\frac{d\bar{N}}{d\phi} = \frac{N}{2\pi} \left(1 + 2 \sum_{n=1}^{\infty} v_n \cos(n(\phi - \Psi_n)) \right). \quad (1.5)$$

where N is the particle yield, ϕ is the azimuthal angle in the transverse plane and Ψ_n is the orientation of the n^{th} order symmetry plane and is called the reaction plane. The reaction plane, along with the participant plane, are shown in Figure 1.7. The coefficient $v_n = \langle \cos[n(\phi_i - \Psi_n)] \rangle$ is the magnitude of the n^{th} order azimuthal anisotropy, and is referred to as the flow harmonic. The first harmonic v_1 is called directed flow because it indicates a particular direction, while the second harmonic v_2 is called elliptic flow since the azimuthal distribution in polar coordinates for $v_2 \neq 0$ is an ellipse. These are shown in Figure 1.8 [66]. The azimuthal correlations that are a result of flow can be described by relativistic hydrodynamics [67, 68]. A comparison of anisotropies measured in terms of v_n in Ref. [69] and a hydrodynamic model described in Ref. [70] is shown in Figure 1.9.

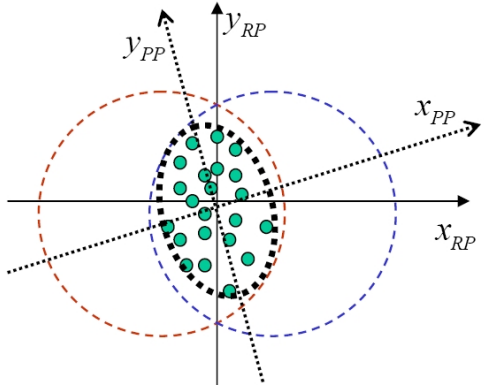


Figure 1.7: Definitions of the Reaction and Participant Plan coordinate systems. Figure taken from Ref. [66].

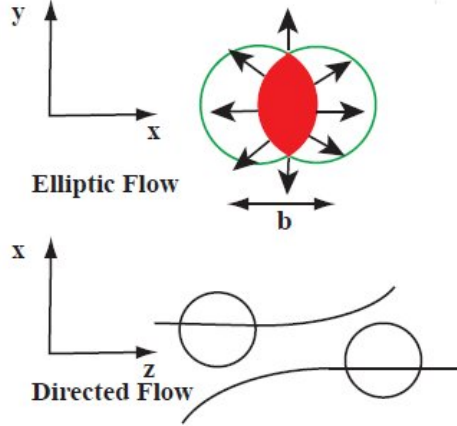


Figure 1.8: Schematics of elliptic and directed flow. Figure taken from Ref. [66].

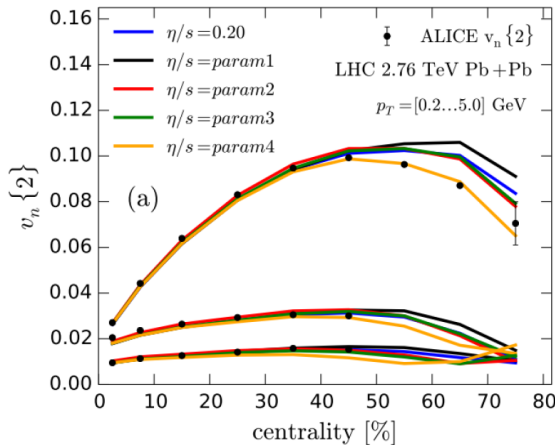


Figure 1.9: Comparison of a hydrodynamic model from [70] to anisotropy measurements by ALICE [69] for different parameterizations of η/s and for different v_n , $n = 2, 3, 4$ from top to bottom, as a function of collision centrality. Figure taken from Ref. [56].

143 The measured anisotropies can be used to constrain the specific viscosity given by the ratio of viscosity
 144 to entropy density, η/s , and have shown that the QGP is a near perfect liquid with an η/s of near the
 145 theoretical minimum of $1/4\pi$ [71, 72]. In fact, this low shear viscosity is what allows the initial fluctuations
 146 in the energy density to survive the chemical freeze-out.

147 1.3 Heavy Ion Collisions

148 Heavy ion collisions are a tool that can be used as a tool to study the quark-gluon plasma (QGP) [33]. In a
 149 heavy ion collision, the colliding nuclei are accelerated to relativistic energies and due to relativistic length
 150 contraction, form discs. In the case of a Pb+Pb collision, the relativistic γ factor is approximately 3000.
 151 Each nucleus contains many colored quarks and antiquarks, with three more quarks than anti-quarks per
 152 nucleon, with the $q\bar{q}$ popping in and out of the vacuum due to quantum fluctuations. These $q\bar{q}$ pairs are
 153 sources of transverse color fields and the corresponding force carriers, the gluons.

154 When these pancake-like discs collide, their color fields interact and there is a color charge exchange,
 155 producing longitudinal color fields that fill the space between the receding discs. The energy densities attained
 156 at RHIC and the LHC are as low as $1\text{GeV}/\text{fm}^3$ [73] and $12\text{GeV}/\text{fm}^3$ [74, 75] respectively, both of which are
 157 above the $0.2 - 1\text{GeV}/\text{fm}^3$ energy density range required to form the QGP [76, 77].

158 After the collision the energy density between the receding nuclei starts to decrease as the QGP cools and
 159 expands. This process, seen in Figure 1.10, continues till the energy density drops to below that within a
 160 hadron and the fluid “hadronizes”. These individual hadrons briefly scatter off of each other before they
 161 freely fly towards the detector (freeze-out).

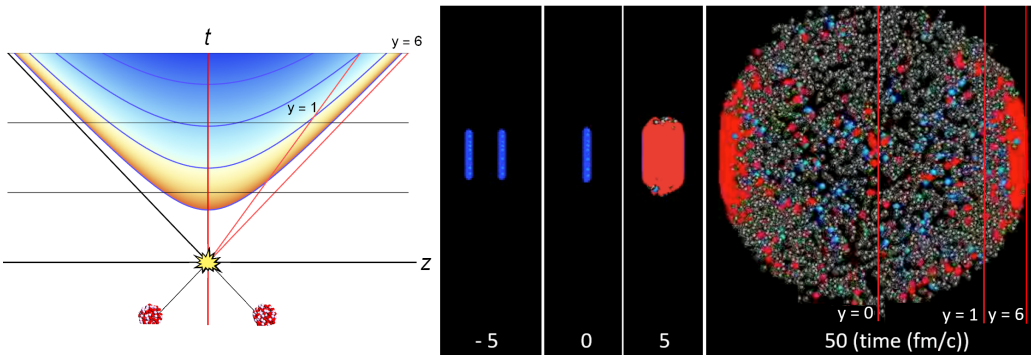


Figure 1.10: (left) Space-time diagram for a heavy ion collision. The color is indicative of the temperature of the QGP formed. (right) Snapshots of a heavy ion collision at $\sqrt{s_{\text{NN}}} = 2.76 \text{ TeV}$ at different times. The Lorentz contracted nuclei are in blue while the QGP is in red. Figure from Reference [56].

162 While Figure 1.10 shows snapshots of a head on (central) collision between two large nuclei, it is possible

163 to have collisions where the impact parameter is larger and hence the overlap region is smaller. These
 164 collisions, called peripheral collisions, qualitatively undergo the same process described above, with the size
 165 and shape of the QGP being different. A schematic of both central and peripheral collisions is shown in
 166 Figure 1.11.

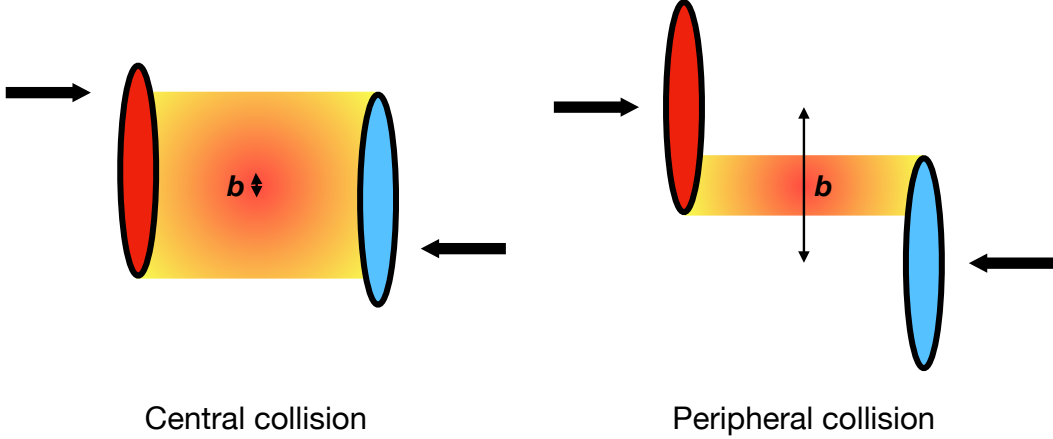


Figure 1.11: A schematic of central (left) and peripheral (right) heavy ion collisions. The impact parameter is given by b .

167 The basic parameters of a heavy ion collision such as the number of participants N_{part} and number of
 168 binary collisions N_{coll} can be determined using the Glauber Monte Carlo simulations [78, 79]. This technique
 169 considers a nucleus-nucleus collision as a collection of independent binary nucleon-nucleon collisions; the
 170 colliding nuclei are modeled as a set of uncorrelated nucleons being positioned within the nucleus based on a
 171 the nuclear density function uniform in azimuthal and in polar angles. The nuclear density function in this
 172 model is a parameterized Fermi distribution given by:

$$\rho(r) = \rho_0 \frac{1 + w(r/R)^2}{1 + e^{\frac{r-R}{a}}} \quad (1.6)$$

173 where ρ_0 is the nucleon density, R is the nuclear radius, a is the skin depth, w corresponds to deviations
 174 from a circular shape and is typically zero for larger nuclei like Cu, W, Au, Pb, and U. For the Pb nuclei
 175 used at the LHC, $w = 0$, $R = 6.62$ fm and $a = 0.55$ fm [80]. The nuclear density distribution for Au and Cu
 176 is shown in Figure 1.12.

177 They are then arranged with a random impact parameter b based on the distribution $d\sigma/db = 2\pi b$ and
 178 projected onto the $x - y$ plane as shown in Figure 1.13. They are then made to travel on straight trajectories,
 179 colliding if $d \leq \sqrt{\sigma_{\text{inel}}^{\text{NN}}/\pi}$, where d is the distance between the nucleons in a plane transverse to the beam

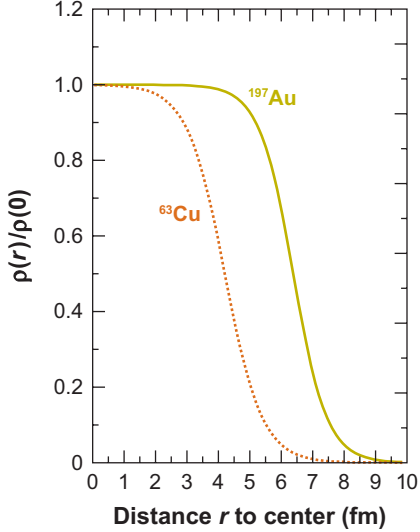


Figure 1.12: The nuclear density distributions for nuclei used at RHIC: Cu ($w = 0$, $R = 4.2$ fm and $a = 0.48$ fm) and Au ($w = 0$, $R = 6.38$ fm and $a = 0.535$ fm) [80]. Figure taken from Ref. [81].

¹⁸⁰ axis and $\sigma_{\text{inel}}^{\text{NN}}$ is the inelastic scattering cross section [81, 82].

¹⁸¹ An important parameter for colliding nuclei A and B with A and B nucleons is the thickness function
¹⁸² T_{AB} . It describes the effective overlap area in which specific nucleons in the two colliding nuclei can interact.
¹⁸³ It can be defined in terms of the probability per unit area of a given nucleon being located at a particular
¹⁸⁴ distance s within the nucleus. For the colliding nuclei A and B, this is given by $T_A(\mathbf{s}) = \int \rho_A(\mathbf{s}, z_A) dz_A$ and
¹⁸⁵ $T_B(\mathbf{s}) = \int \rho_B(\mathbf{s}, z_B) dz_B$. Then, T_{AB} is given by

$$T_{AB}(\mathbf{b}) = \int T_A(\mathbf{s})T_B(\mathbf{s} - \mathbf{b}) d^2 s \quad (1.7)$$

¹⁸⁶ The probability of then having n interactions between nuclei A and B is given by the binomial distribution:

$$P(n, \mathbf{b}) = \binom{AB}{n} \left[T_{AB}(\mathbf{b}) \sigma_{\text{inel}}^{\text{NN}} \right]^n \left[1 - T_{AB}(\mathbf{b}) \sigma_{\text{inel}}^{\text{NN}} \right]^{AB-n} \quad (1.8)$$

¹⁸⁷ where the first term is the number of combinations for finding n collisions from AB possibilities, the second
¹⁸⁸ term is the probability for having exactly n collisions, and the last term the probability of $AB - n$ misses.
¹⁸⁹ Then the total probability of an interaction between A and B is:

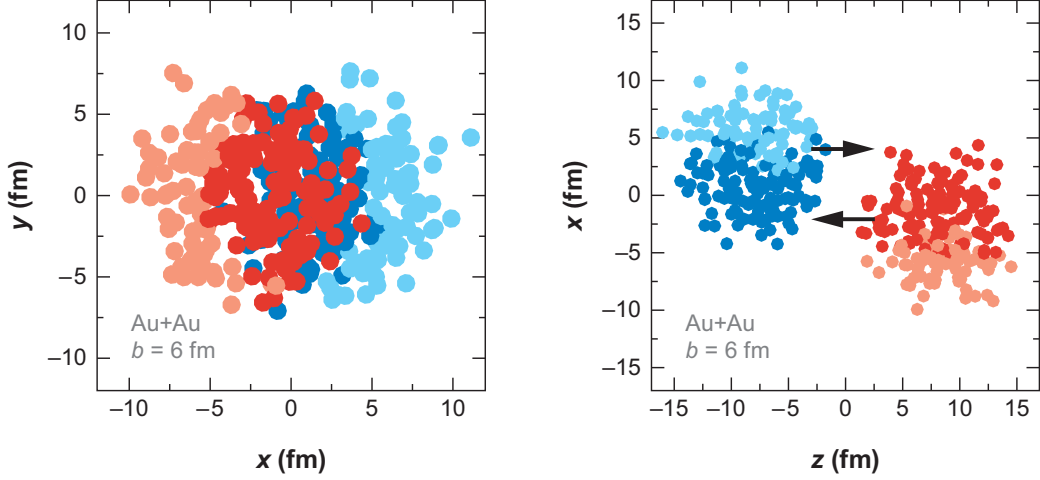


Figure 1.13: A Glauber Monte Carlo event for $Au + Au$ at $\sqrt{s_{NN}} = 200$ geV with impact parameter of 6 fm viewed in the (left) transverse plane and (right) along the beam axis. Darker circles represent the participating nucleons. Taken from [81].

$$\frac{d^2\sigma_{\text{inel}}^{\text{AB}}}{db^2} \equiv p_{\text{inel}}^{\text{AB}}(b) = \sum_{n=1}^{AB} P(n, \mathbf{b}) = 1 - \left[1 - T_{AB}(\mathbf{b})\sigma_{\text{inel}}^{\text{NN}} \right]^{AB} \quad (1.9)$$

190 Then the total cross section is given by

$$\sigma_{\text{inel}}^{\text{AB}} = \int_0^\infty 2\pi b db \left[1 - \left(1 - T_{AB}(\mathbf{b})\sigma_{\text{inel}}^{\text{NN}} \right)^{AB} \right] \quad (1.10)$$

191 and N_{coll} and N_{part} are given by [83, 84]:

$$N_{\text{coll}}(b) = \sum_{n=1}^{AB} n P(n, b) = AB \times T_{AB}(b)\sigma_{\text{inel}}^{\text{NN}} \quad (1.11)$$

$$N_{\text{part}}(b) = A \int T_A(\mathbf{s}) \left[1 - \left(1 - T_B(\mathbf{s} - \mathbf{b})\sigma_{\text{inel}}^{\text{NN}} \right)^B \right] d^2 s + B \int T_B(\mathbf{s} - \mathbf{b}) \left[1 - \left(1 - T_A(\mathbf{s})\sigma_{\text{inel}}^{\text{NN}} \right)^A \right] d^2 s \quad (1.12)$$

192 The correlation between N_{coll} and N_{part} can be seen in Figure 1.14. The charged particle multiplicity N_{ch}
 193 along with the combination of N_{part} and impact parameter b can be used to determine the centrality of a
 194 heavy ion event. An example of this is shown in Figure 1.15.

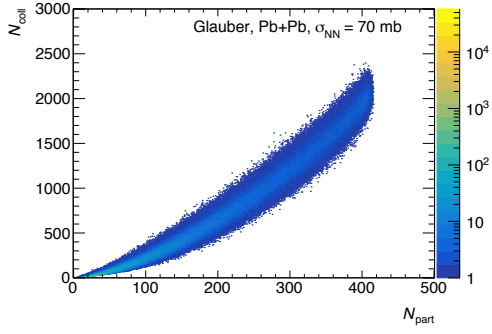


Figure 1.14: The $N_{\text{coll}} - N_{\text{part}}$ correlation for Pb+Pb collisions at $\sqrt{s_{\text{NN}}} = 5.02$ TeV. Taken from [85].

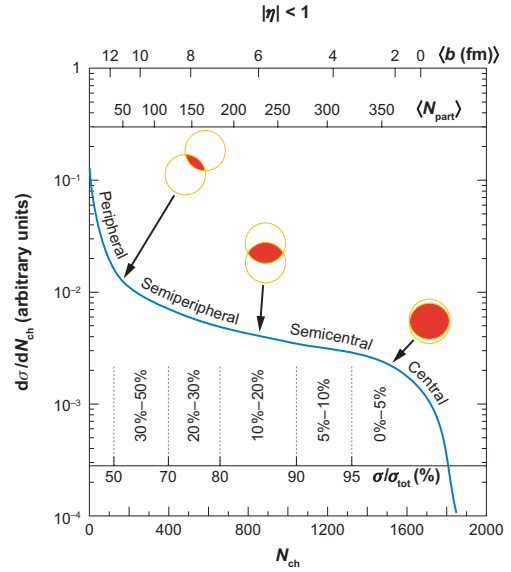


Figure 1.15: The correlation between the observable N_{ch} and N_{part} to determine the centrality distribution. Taken from [81].

195 1.4 Jets and Jet Quenching

196 As colored objects start to fly apart in a particle collision, the energy required to separate them increases as
 197 a natural consequence of color confinement. If the energy with which they are flying apart is greater than the
 198 energy required to separate them, it becomes more favorable to produce a quark-antiquark ($q\bar{q}$) pair. This
 199 process of $q\bar{q}$ production continues recursively until it is not energetically favorable to do so, with the end
 200 result being conical sprays of hadrons called jets. This picture is qualitatively supported by Lattice QCD
 201 [86]. A schematic of this process is shown in Figure 1.16. Because of their color charge, gluon led jets have a
 202 softer fragmentation and result in more particles carrying lesser energy as compared to quark led jets [87].

203 1.4.1 Jets in e^+e^- collisions

204 The simplest process that can be used to study jets is the process $e^+e^- \rightarrow q\bar{q} \rightarrow 2$ jets. The electron and
 205 positron annihilates to produce a photon that can decay into a $q\bar{q}$ pair, that hadronize and form jets. In
 206 fact, this was the process that provided experiment evidence of jets at SPEAR (Stanford Positron Electron
 207 Accelerating Ring) at SLAC in 1975, where it was observed that the distribution of final state hadrons
 208 was not isotropic [88, 89]. Analyses of these distributions showed that they were associated with spin 1/2
 209 quarks. Jets in e^+e^- collisions further provided the first indirect evidence of gluons when three jet events
 210 were observed in the $\Upsilon \rightarrow ggg$ decay [90, 91]. At the Large Electron-Positron Collider (LEP), higher collision

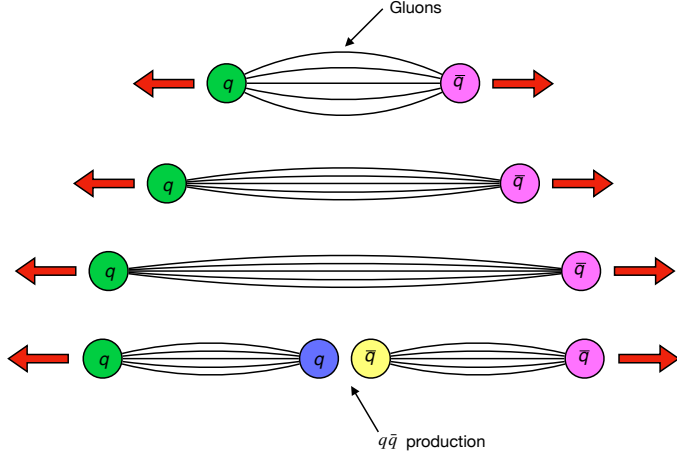


Figure 1.16: A schematic of how jets are produced from a hard process involving $q\bar{q}$. The gluonic flux tubes build up and break as the quarks gain energy, and result in the formation of new $q\bar{q}$ pairs.

211 energies allowed the $e^+e^- \rightarrow Z^0 \rightarrow q\bar{q}$ process. In these processes, to leading order, the $q\bar{q}$ pair evolved via
212 gluon radiation before converting to hadrons [92], allowing for events with more than two jets. Jet production
213 in e^+e^- collisions is also one of the best ways to test the validity of perturbative QCD [93].

214 1.4.2 Jets in pp collisions

215 Jet production in a vacuum is well described in context of perturbative QCD [94]. Processes involving large
216 momentum transfers like high p_T hadron production are shown in Figure 1.17 ².

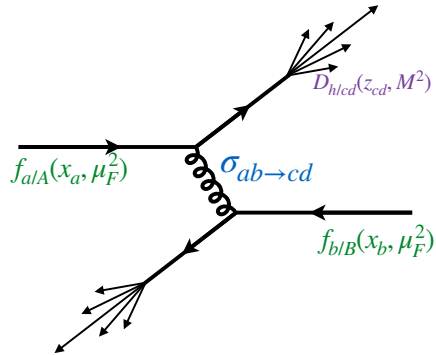


Figure 1.17: Jet production from the process $pp \rightarrow hX$, factorizing in terms of the parton distribution functions, scattering cross sections, and jet fragmentation functions [95].

217 These processes can be described to leading order by perturbative QCD in terms of the parton distribution
218 functions, scattering cross sections, and final state fragmentation functions as [95]:

²In the context of a particle collision, the p_T of a particle is the momentum it carries in a direction perpendicular to the beam axis. It is given by $p_T = |p| \sin \theta$ where θ is the angle of the particle with respect to the beam axis.

$$\begin{aligned}
d\sigma_{pp \rightarrow hX} &\approx \sum_{abjd} \int dx_a \int dx_b \int dz_j f_{a/p}(x_a, \mu_f) \otimes f_{b/p}(x_b, \mu_f) \\
&\quad \otimes d\sigma_{ab \rightarrow jd}(\mu_f, \mu_F, \mu_R) \\
&\quad \otimes D_{j \rightarrow h}(z_j, \mu_f)
\end{aligned} \tag{1.13}$$

where $x_a = p_a/P_A, x_b = p_b/P_b$ are the initial momentum fractions carried by the interacting partons, $z_j = p_h/p_j$ is the momentum fraction carried by the final observed hadron. $f_{a/p}(x_a, \mu_f)$ and $f_{b/p}(x_b, \mu_f)$ are the two parton distribution functions (PDFs), $d\sigma_{ab \rightarrow jd}(\mu_f, \mu_F, \mu_R)$ is the differential cross section for parton scattering and $D_{j \rightarrow h}(z_j, \mu_f)$ is the fragmentation function (FFs) for parton j to hadron h . μ_f and μ_F are the factorization scales and μ_R is the renormalization scale. These are typically taken to be the same hard scale Q , given by the hadron p_T . The PDFs, measured via DIS experiments, characterize the initial state and represent the probability of finding a parton with longitudinal momentum fraction x (shown in Figure 1.18) in the initial hadron, while the FFs describe the probability of fragmenting to a hadron h with given kinematic properties.

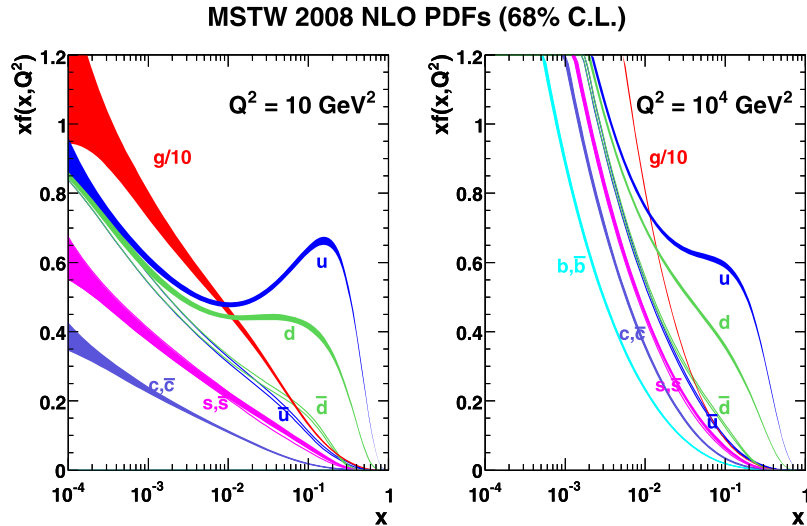
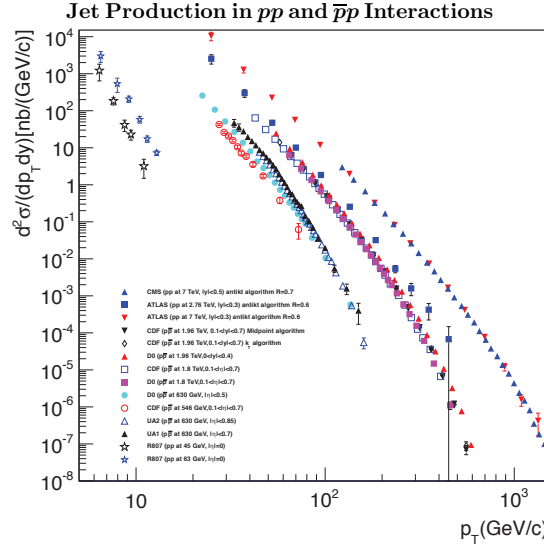
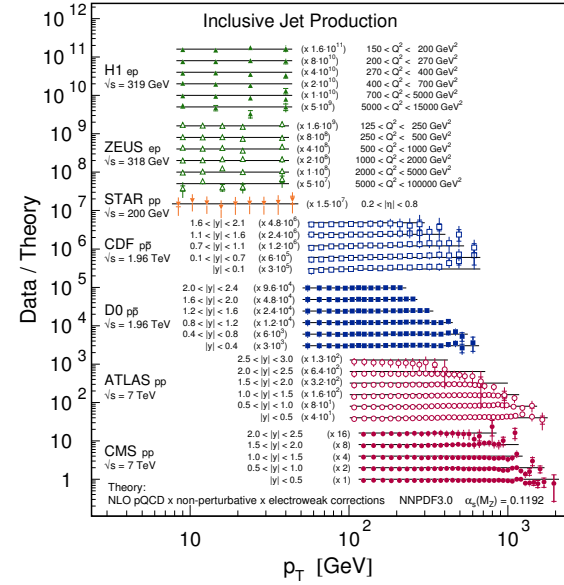


Figure 1.18: The next to leading order (NLO) PDFs at (left) $Q^2 = 10 \text{ GeV}^2$ and (right) $Q^2 = 10^4 \text{ GeV}^2$. The band is the associated one-sigma (68%) confidence level uncertainty. Taken from [96].

The factorization of the jet production process is crucial because it allows for independently measuring and calculating the different components of the cross sections [97]. Jet cross sections in pp and $p\bar{p}$ collisions measured by a variety of different experiments are shown in Figure 1.19(a). A comparison of the measured jet



(a) Inclusive differential jet cross sections shown as a function of jet transverse momentum from different experiments. Figure taken from Ref. [98].



(b) Ratios of data over theory for some jet cross sections measured by different experiments. The next to leading order predictions are derived using the NNPDF3.0 PDF set. Figure taken from Ref. [99].

Figure 1.19: (Left) Some inclusive jet cross sections in data (left) and their comparison to theory (right).

cross sections to theory calculations is shown in Figure 1.19(b). This in particular enables direct comparisons of jet observables in pp collisions to those in heavy ion collisions and determine their modifications.

1.4.3 Jets in heavy ion collisions

In the case of heavy ion collisions, after accounting for geometric scaling effects by the nuclear thickness function as mentioned in Section 1.3, jet observables can be modified due to two sources: the nuclear PDF being distinct from a proton PDF, and the formation of the quark gluon plasma. The former is collectively referred to as cold nuclear matter (CNM) effect, and can be quantified by defining a nuclear modification factor for the PDF:

$$R_a^A(x, Q^2) = \frac{f_{a/A}(x, Q^2)}{f_{a/p}(x, Q^2)} \quad (1.14)$$

where $f_{a/A}$ and $f_{a/p}$ are the nuclear and proton PDFs respectively. This R_a^A factor is determined by global fits to data from DIS measurements [100–102]. CNM effects include the following contributions:

- Shadowing: This is a destructive interference effect that reduces the interactions of a nucleon incident

on a nucleus within its interior and on its back face. This effect reduces the effective number of nucleons in an inelastic interaction to $A^{2/3}$. For Q^2 of the order of a few GeV^2 , this effect dominates for $x < 0.05$ and implies $R_a^A(x, Q^2) < 1$ [103].

- Anti-shadowing: This compensates for the shadowing effect based on the momentum sum rule, and for Q^2 of the order of a few GeV^2 implies $R_a^A(x, Q^2) > 1$ over the region $0.05 < x < 0.20$.
- EMC: The modification of the nuclear structure function was first observed by the European Muon Collaboration [104]. Recent observations have suggested that the effect is caused by short-range correlated nucleon pairs within nuclei [105]. For Q^2 of the order of a few GeV^2 , this effect dominates for $0.2 < x < 0.80$ and implies $R_a^A(x, Q^2) < 1$.
- Fermi Motion: This effect considers the motion of the nucleons within the nucleus. It results in $R_a^A(x, Q^2) > 1$ over the $x > 0.8$ region for Q^2 of the order of a few GeV^2 [106].

Cold nuclear matter effects are experimentally measured using $p + A$ systems where the size and shape of the plasma, and hence any effects thereof, are a lot smaller.

The second source of modification is the formation of the hot and dense quark gluon plasma. The hot nuclear matter effects further serve as an independent confirmation that the medium formed is strongly interacting. Jets are formed early enough that they traverse the Quark Gluon Plasma and as strongly interacting particles, are both affected by, and affect the QGP. This interaction typically results in the jet losing energy and forward momentum [107, 108], with the lost energy being deposited in the medium [109]. Jets can also pick up momentum transverse to the parton direction [110]. The hot nuclear matter effects can be considered to be a combination of collisional and radiative energy losses summarized in Figure 1.20.

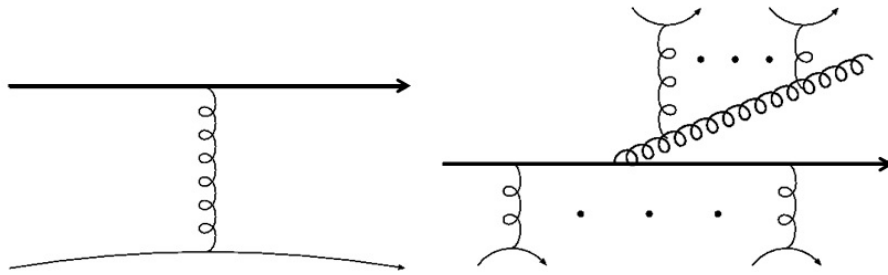


Figure 1.20: The typical diagrams for (left) collisional and (right) radiative energy losses for a parton in a hard scattering as it propagates through the QGP. Taken from [95]

- Collisional energy loss: This is a combination of elastic and inelastic collisions of the hard parton with the constituents of the quark gluon plasma.

- 264 • Radiative energy loss: This is the larger source of parton energy loss and jet quenching. These are
 265 modified by the presence of the plasma due to scatterings off of the plasma constituents. A variety of
 266 radiative energy loss frameworks that have been developed include: Baier-Dokshitzer-Mueller-Peigne-
 267 Schiff-Zakharov (BDMPS-Z) [111], Gyulassy, Levai and Vitev (GLV) [112], Amesto-Salgado-Wiedemann
 268 (ASW) [113], Arnold-Moore-Yaffe (AMY) [114] and higher twist (HT) [115].

Both hot and cold nuclear matter effects can be described by modifying Equation 1.13 as:

$$\begin{aligned} d\sigma_{AB \rightarrow hX} \approx & \sum_{abjj'd} f_{a/A}(x_a) \otimes f_{b/B}(x_b) \\ & \otimes d\sigma_{ab \rightarrow jd}(\mu_f, \mu_F, \mu_R) \\ & \otimes P_{j \rightarrow j'} \\ & \otimes D_{h \rightarrow j'}(z_j, \mu_f) \end{aligned} \quad (1.15)$$

269 where the additional $P_{j \rightarrow j'}$ describes the interaction of the hard parton with the colored medium. This is
 270 typically taken as part of the fragmentation modification as:

$$\tilde{D}_{h \rightarrow j'}(z_j, \mu_f) \approx \sum_{j'} P_{j \rightarrow j'}(p_{j'}|p_j) \otimes D_{h \rightarrow j'}(j') \quad (1.16)$$

271 1.4.4 Jet Algorithms

272 Jet algorithms map the momenta of final state particles into the momenta of jets, and form a core component
 273 of any jet measurement. They can be broadly categorized as sequential recombination and cone algorithms
 274 [116].

275 Cone algorithms cluster particles in the $\eta - \phi$ space ³ assuming that the particles of a jet will be located
 276 in a conical region of the detector. Some examples of cone algorithms are: iterative cone - progressive removal
 277 (IC-PR) [117], iterative cone - split merge (IC-SM) [118], and SISCone [119].

278 Sequential recombination algorithms on the other hand work by grouping particles in momentum space,
 279 with the result that they have fluctuating areas in $\eta - \phi$ space. Some examples of these algorithms are: k_t
 280 [120], anti- k_t [121], and Cambridge/Aachen (C/A) [122].

281 Recombination algorithms have an advantage over the cone algorithms in that they are infrared and

³ $\eta = -\ln[\tan(\theta/2)]$ is the pseudorapidity and is a spatial coordinate that describes the angle θ of a particle with respect to the beam axis. ϕ is the azimuthal angle around the beam axis. The coordinate system of detectors is typically based on the $\eta - \phi$ plane.

282 collinear safe (IRC). This is related to instabilities in the cones that are found due to soft radiation. In a
 283 collinear safe jet algorithm, the presence of a virtual loop or a collinear splitting of a central particle would
 284 not change the number of jets being reconstructed. On the other hand, while a collinear unsafe jet algorithm
 285 would not change its output with the presence of a virtual loop, a splitting in the central particle would
 286 lead to the left and right most particles forming individual seeds, implying two reconstructed jets [123].
 287 Figure 1.21 describes the collinear safety problem.

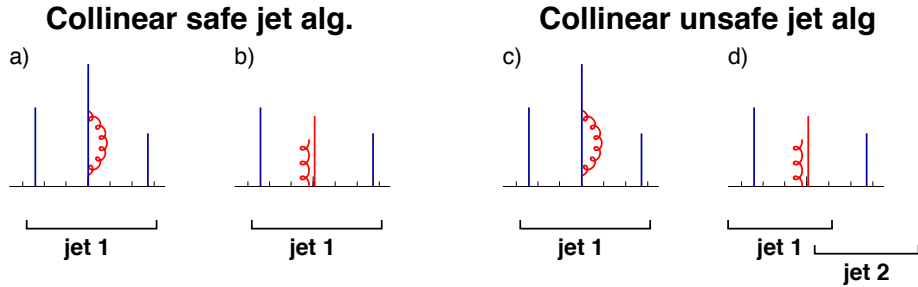


Figure 1.21: An illustration of collinear unsafe behavior. The particle p_T is proportional to the height and the horizontal axis indicates rapidity. Taken from [123].

288 A schematic describing infrared safety problem is shown in Figure 1.22. Here an infrared safe algorithm
 289 would use the three particles as seeds iteratively find two stable cones. An unsafe algorithm however would
 290 find three overlapping cones based on the addition of a soft seed.

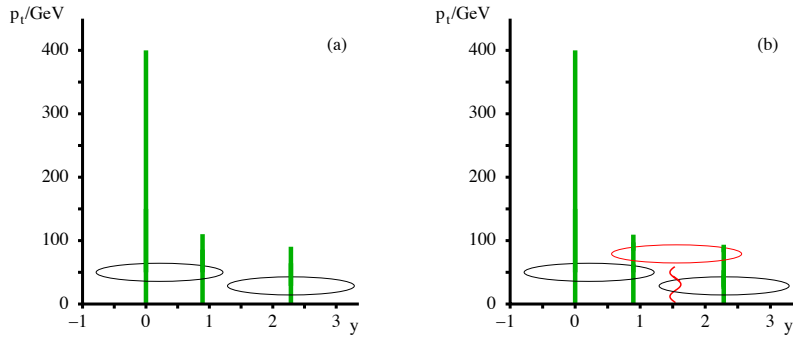


Figure 1.22: An illustration of infrared unsafe behavior. The particle p_T is proportional to the height and the horizontal axis indicates rapidity. Taken from [119].

291 Sequential recombination algorithms are more popular because they are IRC safe and are discussed in
 292 further detail below. The general procedure for sequential recombination algorithms is as follows:

- 293 • Calculate all distances d_{ij} between entities i and j , and distance d_{iB} between entity i and beam B
- 294 • Find the minimum of d_{ij} and d_{iB} :

- 295 ◦ If d_{ij} is the minimum, combine i and j by summing their four-vectors, remove them from the list
 296 of particles and return to beginning.
- 297 ◦ If the smallest distance is d_{iB} , then take i as the jet and remove it from the list of particles and
 298 return to beginning.
- 299 • Continue the procedure till the list of items is empty.

300 In general the distance d_{ij} between the objects is found the via the prescription

$$d_{ij} = \min(k_{Ti}^{2p}, k_{Tj}^{2p}) \frac{\Delta_{ij}^2}{R^2} \quad (1.17)$$

$$d_{iB} = k_{Ti}^{2p} \quad (1.18)$$

301 where k_{Ti} is the transverse momentum of particle i and $\Delta_{ij} = \sqrt{\Delta\eta_{ij}^2 + \Delta\phi_{ij}^2}$ is the distance between particles
 302 i and j in $\eta - \phi$ space. R the distance parameter and reflects the size of the jet being considered.

303 Different recombination algorithms use different values of p . The k_t algorithm has $p = 2$. This results in
 304 clustering soft particles first, with the final jet having a fluctuating area. This algorithm is susceptible to
 305 processes that contribute particles that do not belong to a jet. The C/A algorithm uses $p = 0$. This results
 306 in the distances between particles being completely independent of momentum. The anti- k_t algorithm uses
 307 $p = -1$. Hence, the algorithm clusters hard particles first, making it the least susceptible to background. The
 308 behavior of the different clustering algorithms is shown in Figure 1.23. The anti- k_t algorithm is the default
 309 used in all LHC collaborations.

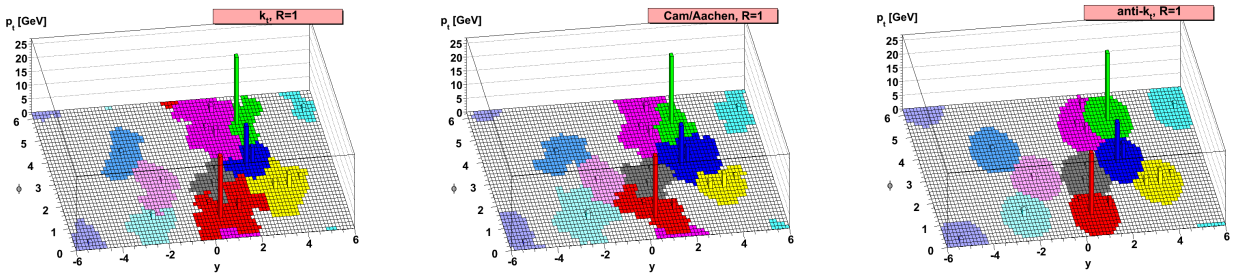


Figure 1.23: Different clustering algorithms applied to the sample parton-level event. Figure taken from [121].

Chapter 2

Major Jet Measurements

310 This chapter shall discuss some important experimental jet measurements that contextualize and motivate
311 the study of the main analysis in this thesis. These include the study of the hadron yields, dijet balance, jet
312 yields, jet fragmentation, and jet profiles.

313 2.1 Hadron Suppression

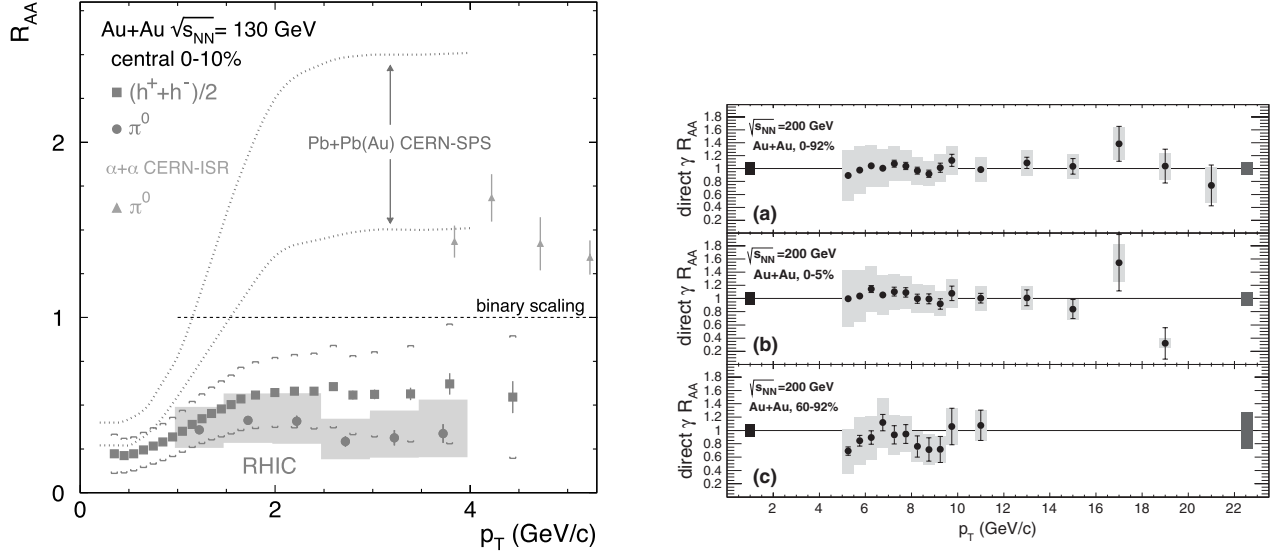
314 This discussion is based on Ref. [125]. Done at RHIC by the PHENIX collaboration, this was one of the
315 first experimental measurements of jet quenching that showed the presence of the QGP. This measurement
316 analyzed high p_T charged hadrons and neutral π^0 s ($p_T > 2\text{GeV}$) from jets produced in Au+Au collisions,
317 collided at $\sqrt{s_{NN}} = 130 \text{ GeV}$. Since jets form early in the collision and experience the evolution of the QGP,
318 they are expected to lose energy due to collisional and radiative losses as discussed in Section 1.4. The
319 modifications between the pp and Au+Au system was quantified by constructing the nuclear modification
320 factor R_{AA} , given as:

$$R_{AA} p_T = \frac{(1/N_{\text{evt}}) d^2 N^{A+A} / dp_T d\eta}{(\langle N_{\text{binary}} \rangle / \sigma_{\text{inel}}^{N+N} d^2 \sigma^{N+N} / dp_T d\eta)} \quad (2.1)$$

321 where N_{evt} is the number of Au+Au events, $\langle N_{\text{binary}} \rangle$ is the average number of binary collisions per event, σ
322 is the scattering cross section, and p_T and η are the kinematics of the charged particle. The R_{AA} for charged
323 hadrons and neutral pions is shown in Figure 2.1(a).

324 A significant depletion is seen, with the R_{AA} rising for $p_T < 2 \text{ GeV}$ and remaining fairly constant
325 thereafter. This modification includes both hot nuclear matter effects from the QGP, as well as cold nuclear
326 matter effects like the Cronin effect that can be seen in $p + A$ collisions [129].

327 Electroweak probes like photons and Z bosons do not lose energy in the QGP since they do not interact
328 strongly, and their R_{AA} is expected to be closer to unity. There can be differences though, that are coming
329 from cold nuclear matter effects. This can be seen in Figure 2.1(b)



(a) The R_{AA} for charged hadrons and neutral pions in Au+Au collisions at $\sqrt{s_{NN}} = 130$ GeV. Also shown is the R_{AA} for inclusive cross sections in $\alpha + \alpha$ compared to pp at $\sqrt{s_{NN}} = 31$ GeV [126] and spectra from Pb+Pb and Pb+AU compared to pp at $\sqrt{s_{NN}} = 17$ GeV [127]. Figure taken from Ref. [125].

(b) The R_{AA} for photons in three centrality regions in Au+Au collisions at $\sqrt{s_{NN}} = 200$ GeV. Figure taken from Ref. [128].

Figure 2.1: R_{AA} evaluated for (left) charged hadrons and pions and (right) photons.

330 2.2 Dijet Balance: x_J

331 This section will discuss the dijet balance as measured by the ATLAS detector for Pb+Pb collisions at
 332 $\sqrt{s_{NN}} = 2.76$ TeV [130]. The dijet imbalance can be expressed in terms of x_J defined as

$$x_J = \frac{p_{T2}}{p_{T1}} \quad (2.2)$$

333 where p_{T2} and p_{T1} are the transverse momenta of the two highest- p_T jets in the event respectively. The
 334 minimum p_{T2} considered is 25 GeV and the pair of jets are separated by $|\Delta\phi| > 7\pi/8$. The dijet yields
 335 normalized by the number of jets and determined as $1/N_{\text{jets}} dN/dx_J$ are presented as a function of x_J for
 336 different centrality intervals, as well as different ranges for p_{T1} . The measured distributions are further
 337 unfolded to remove detector resolution effects and allow comparison to theoretical models.

338 Figure 2.2 shows the x_J distribution for dijet pairs in pp and Pb+Pb collisions in two different centrality
 339 bins and two p_{T1} ranges. It can be seen that the dijet yields in pp are peaked at unity and become narrower
 340 for larger p_{T1} ranges. This reflects the fact that the effects of jet quenching are minimal and the higher- p_T
 341 jets are better balanced. The dijet yields in peripheral Pb+Pb collisions are similar to the distributions from

the pp data, showing that the effects of quenching are smaller. On the other hand, dijet yields in central Pb+Pb collisions are significantly broadened, reflecting the maximal of jet quenching. This is consistent with the picture of the individual jets in the dijet pair traversing different lengths in the QGP and hence losing different amounts of energy. In fact, the distribution for Pb+Pb data is peaked at $x_J = 0.5$, implying a loss of 50% of the jet p_T .

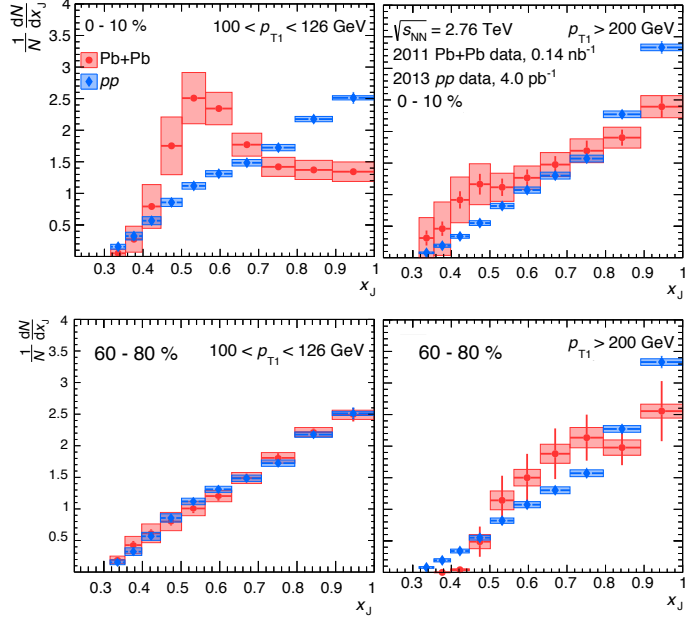


Figure 2.2: The $1/N_{\text{jets}} dN/dx_J$ distributions for $R = 0.4$ jets as a function of x_J for pp (blue) and $\text{Pb}+\text{Pb}$ (red) collisions. The different panels are for (top) central and (bottom) peripheral collisions in (left) $100 < p_{T1} < 126 \text{ GeV}$ and (right) $p_{T1} > 200 \text{ GeV}$. The pp data is the same in all panels. The statistical uncertainties are indicated by the bars while the boxes indicate the systematic uncertainties. Figures taken from [130].

It is further seen that narrower jets are flatter than wider jets. This is consistent with the expectation that the transverse momenta correlation between the dijet pair is weaker for jets with smaller radii due to radiation that is outside the nominal jet cone.

2.3 Modification of jet yields: R_{AA}

This section discusses the measurement of the inclusive jet R_{AA} as measured by the ALICE detector for jets in $\sqrt{s_{\text{NN}}} = 2.76 \text{ TeV}$ Pb+Pb and pp collisions [131].

While measurements that compare jets in a dijet system to each other as discussed in Section 2.2 can provide valuable information about how jets lose energy, they have the following limitation: If both jets lose equal amounts of energy, the dijet yield will still be peaked at unity and no new information will be obtained.

356 Thus, it is useful to compare the jet yields directly between the pp and Pb+Pb systems and construct the jet
 357 R_{AA} observable. This is defined as:

$$R_{AA} = \frac{\frac{1}{N_{\text{evt}}} \left. \frac{d^2 N_{\text{jet}}}{dp_T dy} \right|_{\text{cent}}}{\langle T_{AA} \rangle \left. \frac{d^2 \sigma_{\text{jet}}}{dp_T dy} \right|_{\text{pp}}} \quad (2.3)$$

358 where T_{AA} is the nuclear thickness function and accounts for the geometric enhancement between pp and
 359 Pb+Pb as discussed in Section 1.3 and [81].

The jet spectrum in Pb+Pb events, as well as the jet R_{AA} for central Pb+Pb is shown in Figure ??.

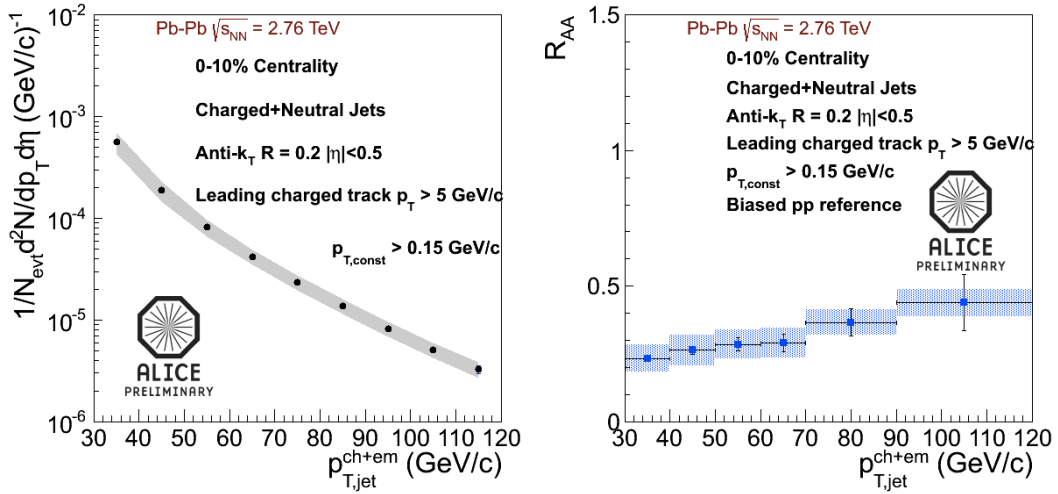


Figure 2.3: (Left) The inclusive jet cross section as a function of jet p_T in 0–10% central Pb+Pb collisions at $\sqrt{s_{\text{NN}}} = 2.76 \text{ TeV}$. The band around the data points represents the systematic uncertainty. (Right) The R_{AA} for 0–10% central Pb+Pb collisions. Figure taken from [131].

360

361 It can be seen that the most central collisions show a clear suppression with an $R_{AA} \approx 0.25$ at jet p_T 30
 362 GeV. The R_{AA} value slowly evolves with jet p_T and rises to 0.5 at jet $p_T = 100$ GeV. This modification
 363 becomes smaller for more peripheral collisions.

364 These observations are consistent with results from ATLAS and CMS [132–134]. The ATLAS results at
 365 $\sqrt{s_{\text{NN}}} = 5.02 \text{ TeV}$ are shown in Figure 2.4(a). The higher collision energy allows access to higher p_T jets. The
 366 smooth centrality dependence can be more clearly seen in Figure 2.4(b), where R_{AA} is shown as a function of
 367 $\langle N_{\text{part}} \rangle$ for jets in the 100–126 GeV and 200–251 GeV ranges. The magnitude of the suppression is also seen to
 368 significantly depend on jet p_T for $\langle N_{\text{part}} \rangle \geq 50$.

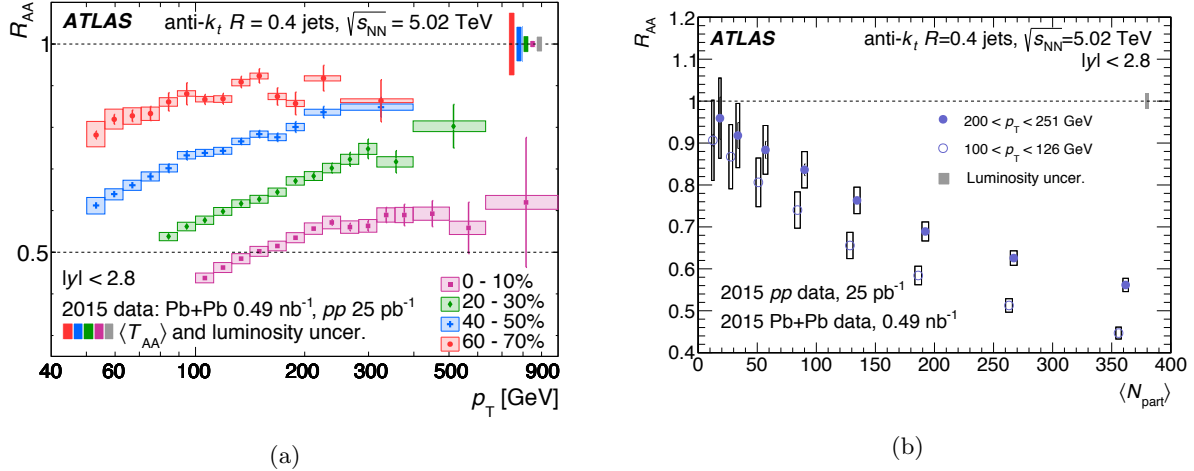


Figure 2.4: (Left) The R_{AA} distributions as a function of jet p_T for different centrality bins and jet rapidity $|y| < 2.8$. (Right) The R_{AA} distributions as a function of jet $\langle N_{\text{part}} \rangle$ for different jet p_T bins and jet rapidity $|y| < 2.8$. Figures taken from [133]

369 2.4 Jet Fragmentation

370 This section will discuss the jet fragmentation as measured by the ATLAS detector for Pb+Pb collisions at
 371 $\sqrt{s_{NN}} = 5.02$ TeV [135]. While measurements of R_{AA} [132, 134, 136] and asymmetry [130, 137, 138] describe
 372 how much energy is lost by the jet, fragmentation measurements describe the momentum distribution of
 373 particles associated to the jet. These can be described as:

$$D(z) = \frac{1}{N_{\text{jet}}} \frac{dn_{\text{ch}}}{dz} \quad (2.4)$$

$$D(p_T) = \frac{1}{N_{\text{jet}}} \frac{dn_{\text{ch}}}{dp_T} \quad (2.5)$$

374 where $z = p_T \cos(\Delta R / p_T^{\text{jet}})$ and gives the charged-particle longitudinal momentum fraction relative to the
 375 jet. Modifications to the fragmentation functions in Pb+Pb collisions can be evaluated by constructing the
 376 ratios $R_{D(z)} = D(z)_{\text{Pb+Pb}} / D(z)_{pp}$ and $R_{D(p_T)} = D(p_T)_{\text{Pb+Pb}} / D(p_T)_{pp}$. This measurement is corrected for
 377 detector effects and unfolded to the particle level. This allows for comparisons to other measurements and
 378 theoretical models. The $D(p_T)$ distribution is shown in Figure 2.5.

379 The modifications to the $D(z)$ and $D(p_T)$ distributions in central (top) and peripheral (bottom) collisions
 380 are shown in Figure 2.6. The shape of these modifications is very similar for both $D(z)$ and $D(p_T)$. There is
 381 an enhancement of particles with low z and p_T , followed by a suppression at intermediate z and p_T , and
 382 finally an enhancement at high z and p_T . These modifications become smaller for more peripheral collisions.

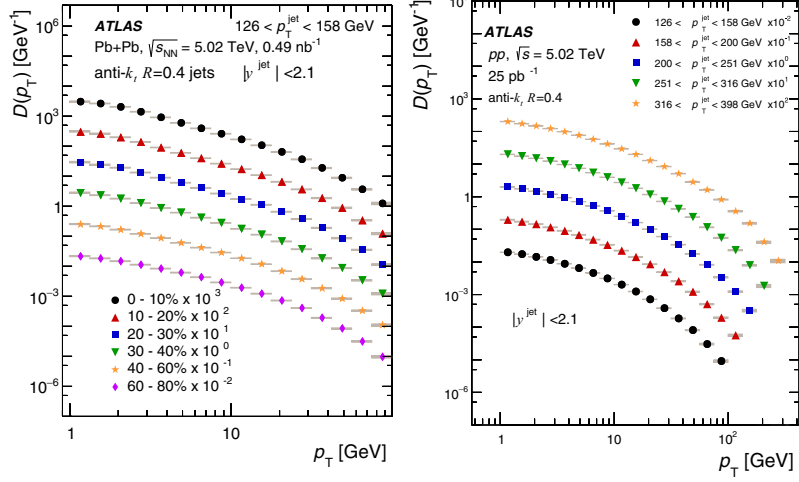


Figure 2.5: (Left) The $D(p_T)$ distributions in pp as a function of charged-particle p_T for different p_T^{jet} selections and for jet rapidity $|y| < 2.1$. (Right) The $D(p_T)$ distributions in $Pb+Pb$ as a function of charged-particle p_T for different centrality selections and for jet rapidity $|y| < 2.1$. The error bars represent statistical uncertainties while the shaded boxes represent systematic uncertainties. Figure taken from [135].

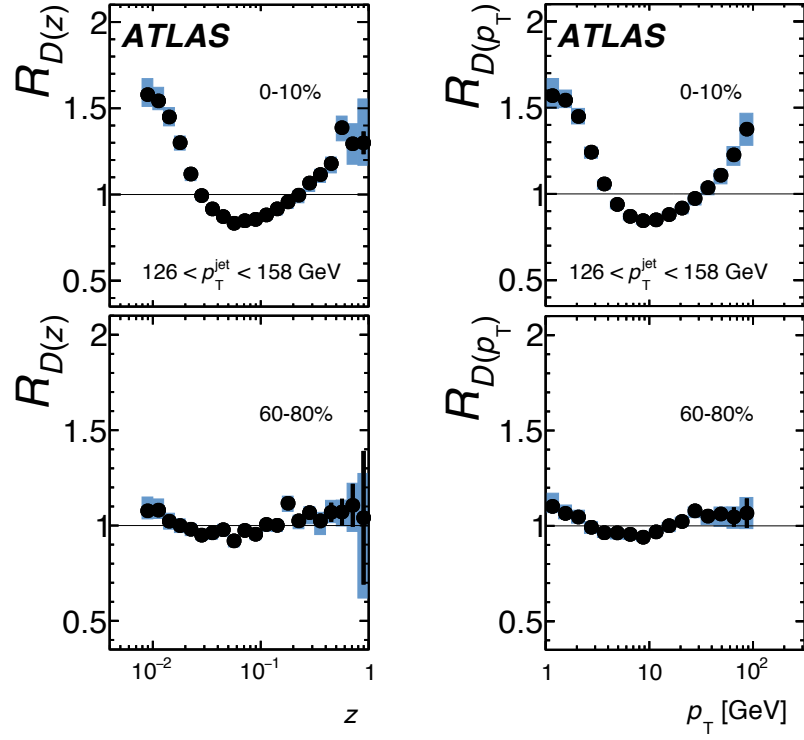


Figure 2.6: The modifications to the (left) $D(z)$ and (right) $D(p_T)$ distributions in (top) 0–10% central and (bottom) peripheral $Pb+Pb$ compared to pp as a function of charged-particle z and p_T respectively. The error bars represent statistical uncertainties while the shaded boxes represent systematic uncertainties. Figures taken from [135].

383 The low momentum excess can be further investigated by calculating the extra number of particles N_{ch} in
 384 Pb+Pb compared to pp as given below:

$$N_{\text{ch}} = \int_{p_{\text{T min}}}^{p_{\text{T max}}} \left(D(p_{\text{T}})_{\text{Pb+Pb}} - D(p_{\text{T}})_{pp} \right) dp_{\text{T}} \quad (2.6)$$

385 where $p_{\text{T min}} = 1$ GeV and $p_{\text{T max}} = 4.2$ GeV.

386 The N_{ch} distributions can be seen in Figure 2.7. It can be clearly seen that the size of the enhancement
 387 in pp compared to pp at low p_{T} increases as a function of $p_{\text{T}}^{\text{jet}}$, growing from about 1.5 to 2.5 extra particles
 388 in the most central Pb+Pb collisions. This excess is even seen in the peripheral Pb+Pb collisions, though it
 389 is a lot smaller and ranges from 0.2 to 0.5 extra particles.

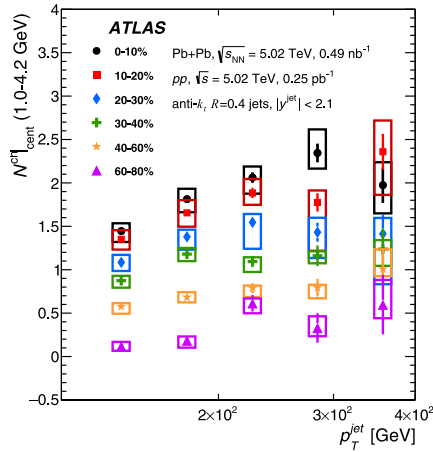


Figure 2.7: The number of extra particles that carry $1 < p_{\text{T}} < 4$ GeV in Pb+Pb compared to pp . The different colors represent different centrality selections. The error bars represent statistical uncertainties while the shaded boxes represent systematic uncertainties. Figure taken from [135].

390 The modifications to the $D(z)$ distributions have also been compared to a variety of models, including
 391 the Effective Quenching model [139], the Soft Collinear Effective Theory [140, 141], and the Hybrid Model
 392 [142]. These comparisons are shown in Figure 2.8, and are discussed in detail in Chapter 3.

393 2.5 Jet Profile

This section will discuss the momentum profile of the jet as measured by the CMS detector for Pb+Pb collisions at $\sqrt{s_{\text{NN}}} = 5.02$ TeV [143]. This can be considered to be an extension to a fragmentation function measurement in that it provides information about the momentum distribution of charged particles not only

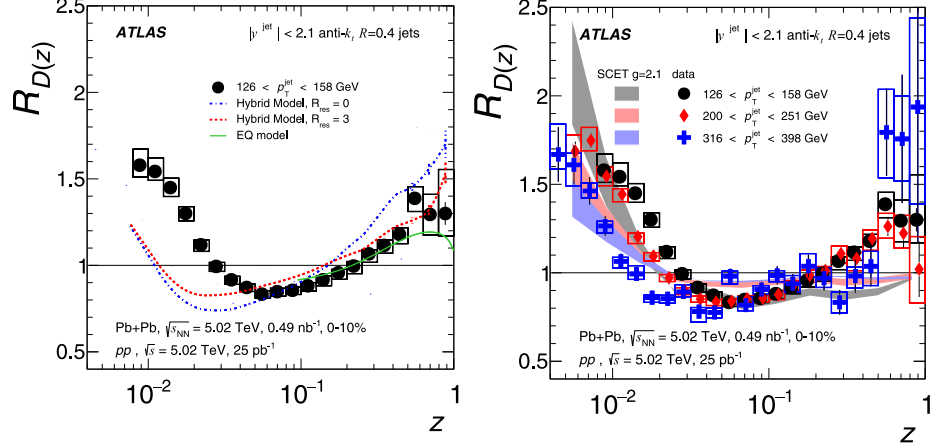


Figure 2.8: The $R_{D(z)}$ distributions compared to the EQ and Hybrid models (left) and SCET (right). The error bars represent statistical uncertainties while the shaded boxes represent systematic uncertainties. Figure taken from [135].

within the jet boundary, but also outside. The jet profile is defined as the distribution of particle yields in an annulus of width Δr and is given as:

$$P(\Delta r) = \frac{1}{\delta r} \frac{1}{N_{\text{jet}}} \sum_{\text{jets}} \sum_{\text{tracks} \in (\Delta r_a, \Delta r_b)} p_{\text{T}}^{\text{trk}} \quad (2.7)$$

394 where Δr_a and Δr_b are the edges of the annulus at ΔR , and $\delta r = \Delta r_b - \Delta r_a$.

395 The jet profile for pp , $Pb+Pb$, and the modification to the jet shape variable are shown in Figure 2.9.

396 It can be seen from the bottom panels of Figure 2.9 that there is an excess of low p_{T} particles in $Pb+Pb$
397 compared to pp at intermediate and large distances from the jet axis. This enhancement is compensated by
398 a depletion of high p_{T} particles ($p_{\text{T}} > 4$ GeV) at all angles. In particular, the depletion in particle yields
399 in 0–10% central $Pb+Pb$ is up to almost half the particle yields in pp for $\Delta r > 0.4$. The modifications be
400 described in terms of jet quenching, coupled with effects from the wake the jet as it propagates through the
401 QGP. This wake can cause an enhancement in the low p_{T} yield of particles that is most easily seen at large
402 angles.

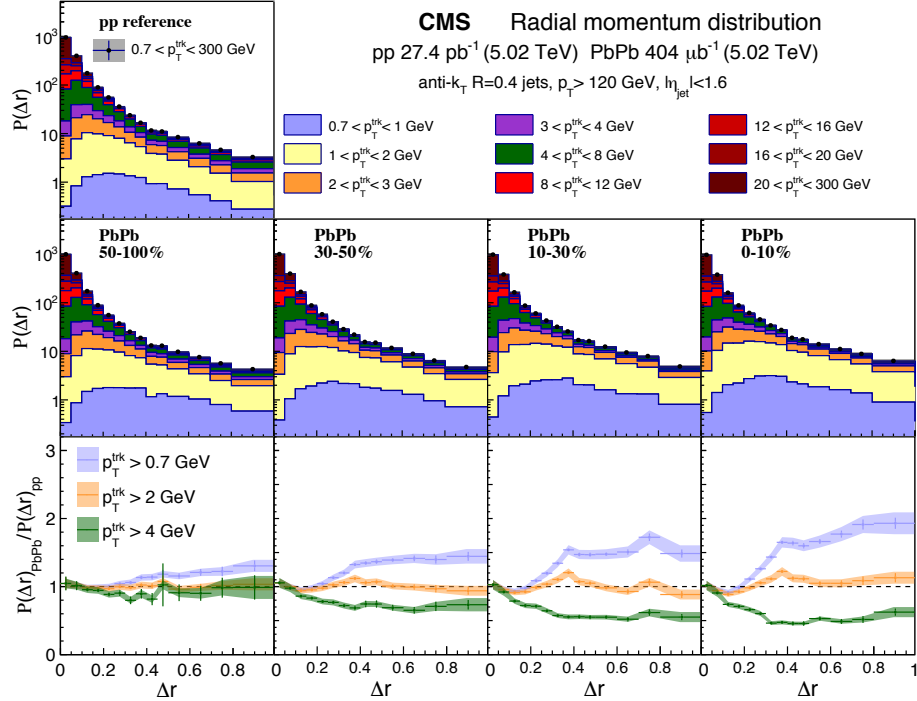


Figure 2.9: The jet profile in pp (top) and Pb+Pb (middle) as a function of distance from the jet axis. The different panels in the middle give the jet shape distribution for different centrality intervals. The modifications to the jet shape are shown at the bottom, with each panel corresponding to a different centrality. Figure taken from [143].

Chapter 3

Jet Energy Loss Models

403 This chapter shall discuss a few models that have been used to explain the data, looking in particular at the
404 following: Effective Quenching (EQ), Soft Collinear Effective Theory (SCET), Hybrid Model, and Jet Fluid
405 Model. These models form the backdrop in which the main thesis analysis was conducted.

406 3.1 Effective Quenching

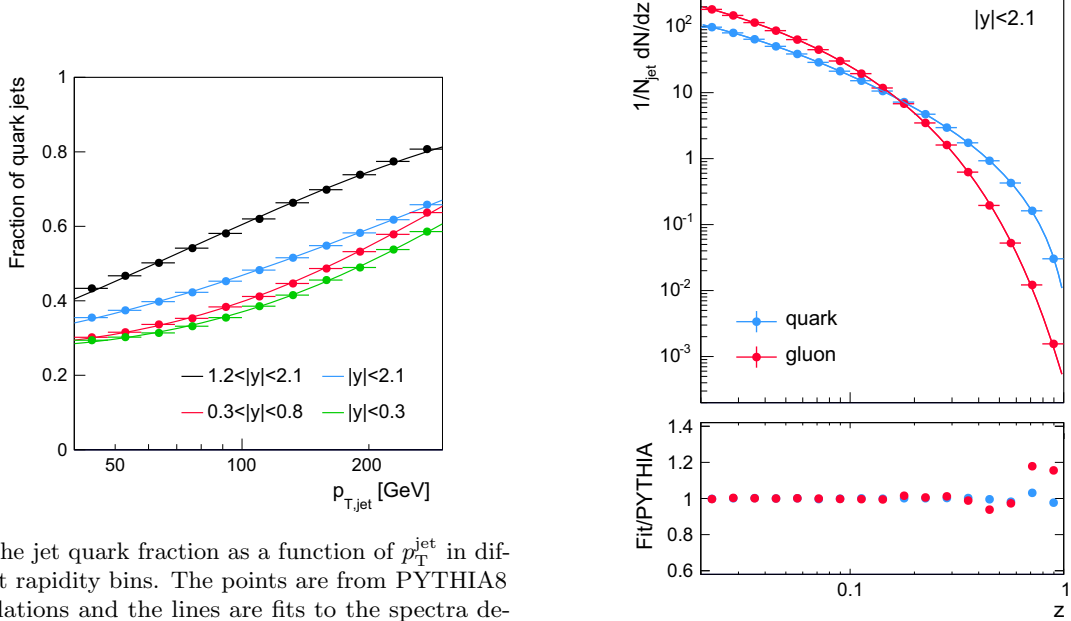
407 This discussion is based on the model introduced in Ref. [139]. This phenomenological model emphasizes
408 the jet p_T dependence of the quark to gluon fraction and the difference between quark-jet and gluon-jet
409 quenching. It uses an “extended” power law parameterization of the high- p_T hadron spectra coupled with a
410 quenching that is based on a non-constant fractional energy loss. This model considers the different color
411 charges carried by quarks and gluons and their different splitting functions, and assumes that gluon jets lose
412 energy at a rate 9/4 times higher than quark jets. The key assumption of the model are:

- 413 • The energy lost by a jet is radiated at large angles and does not appear within the jet cone. This is
414 backed by [137].
- 415 • The fragmentation pattern of the jet is unaffected by the presence of the QGP i.e. they fragment as
416 they would in a vacuum. This is motivated by the idea that the QGP is unable to resolve the internal
417 jet structure and is supported by [144, 145].

418 The model uses the following extended power-law parameterization to describe the high- p_T jet spectra:

$$\frac{dn}{dp_T^{\text{jet}}} = A \left(\frac{p_{T_0}}{p_T^{\text{jet}}} \right)^{n+\beta \log(p_T^{\text{jet}}/p_{T_0})} \quad (3.1)$$

419 where p_{T_0} is a reference transverse momentum at which $A = dn/dp_T^{\text{jet}}$, β is the logarithmic derivative of
420 dn/dp_T^{jet} at $p_T^{\text{jet}} = p_{T_0}$. Then the combined spectrum from quarks and gluons can be written in terms of



(a) The jet quark fraction as a function of p_T^{jet} in different rapidity bins. The points are from PYTHIA8 simulations and the lines are fits to the spectra determined using Equation 3.1.

(b) A comparison of the quark and gluon fragmentation. The points are from PYTHIA8 simulations and the lines are fits to those points using Equation 3.2.

Figure 3.1: Fits to quark fractions and fragmentation functions from PYTHIA8. Figure taken from [139].

421 Equation 3.1 with weighted contributions from the different quark and gluon fractions, f_{q0} and $f_{g0} = 1 - f_{q0}$
422 respectively.

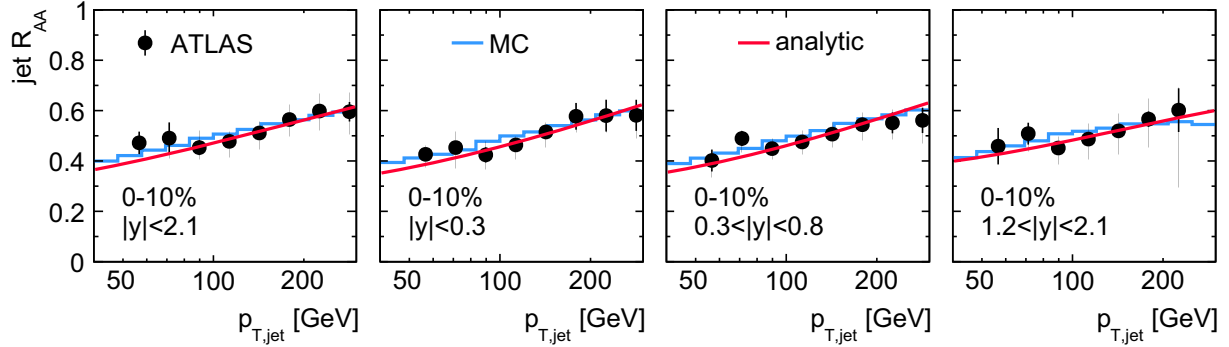
423 The p_T dependence of the quark fraction along with the fit is shown in Figure 3.1(a). The fragmentation
424 functions can also be determined using final-state charged hadrons within a $R = 0.4$ jet cone. These are fit
425 to the form $D(z)$, with fits for the quark and gluon fragmentation shown in Figure 3.1(b).

$$D(z) = a \times \frac{(1 + dz)^b}{(1 + ez)^c} \times e^{-fz} \quad (3.2)$$

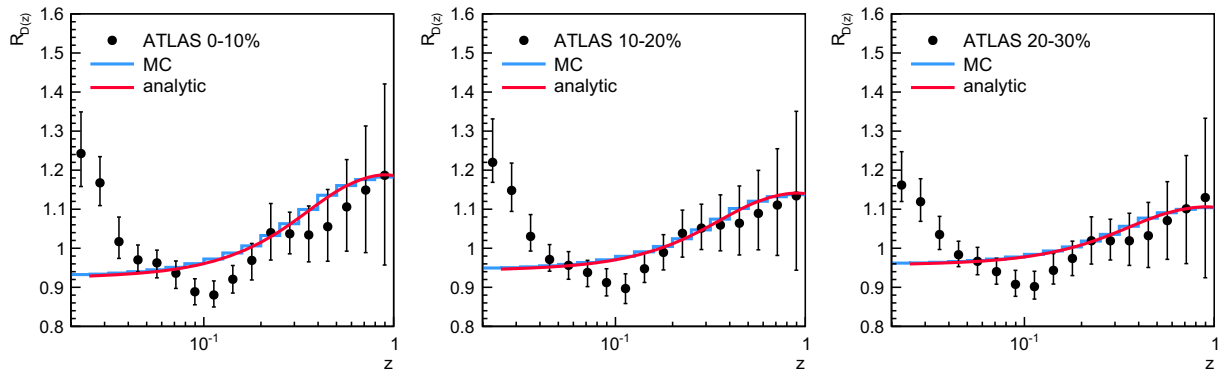
426 For the quenched spectra, this model assumes a non-constant fractional shift given below as S . This
427 approach is based on [146] and is used because of the inability of the constant fractional shift to explain the
428 jet p_T dependence of measured R_{AA} .

$$S = s' \left(\frac{p_T^{\text{jet}}}{p_{T0}} \right)^\alpha \quad (3.3)$$

429 where α is an undetermined parameter and s' is the shift for a jet with $p_T^{\text{jet}} = p_{T0}$. The fractional shift can



(a) A comparison of the R_{AA} as measured by ATLAS for central Pb+Pb collisions in [132], a MC calculation (blue) and the analytic calculation (red) in the EQ model with the extended power-law parameterization and a non-constant fractional energy loss. The different panels are different rapidity intervals.



(b) A comparison of the $R_{D(z)}$ as measured by ATLAS in [147], a MC calculation (blue) and the analytic calculation (red) in the EQ model with the extended power-law parameterization and a non-constant fractional energy loss. The different panels are different centrality intervals.

Figure 3.2: A comparison of measured data, MC, and the analytic calculation of the EQ model. Figure taken from [139].

430 be coupled with Equation 3.1 and the quark and gluon fractions to give a functional form of the quenched
 431 high- p_T hadron spectra for quarks and gluons. This can be further used to construct a jet R_{AA} that is fit to
 432 data and is shown in Figure 3.2(a). It can be seen that the analytic fits and the MC are in good agreement.
 433 While the fits agree with the data by definition, the robustness of the model can be seen in that it describes
 434 the data with a single value for α and a simple centrality dependent shift constant s' .

435 Fits to the $D(z)$ distributions are shown in Figure 3.2(b) and it can be seen that while the MC and
 436 analytic calculation agree well with each other, they are only able to qualitatively capture some features of
 437 the data. The enhancement at high z can be explained by an increased quark content of the jet spectrum
 438 and subsequent differential quenching for quark and gluon jets. The low z enhancement on the other hand
 439 can be considered to be a result of a gluon radiation within the jet or a wake from the medium itself.

440 3.2 Jet Fluid model

441 This discussion is based on the model introduced in Ref. [148]. This model considers the evolution of the jet
 442 and QGP in a coupled manner, considering the energy and transverse momentum exchange between them.
 443 In this picture, both the jet and medium are allowed to modify each other; the jet is modified via collisional
 444 and radiative processes while the medium evolves hydrodynamically and is modified because it picks up the
 445 energy lost by the jet.

446 The time evolution of the jet is given by a set of coupled transport equations that describe the energy
 447 and transverse momentum distributions of the partons within the jet. These are given as

$$f_i(\omega_i, k_{\text{T}i}^2, t) = \frac{dN_i(\omega_i k_{\text{T}i}^2, t)}{d\omega_i dk_{\text{T}i}^2} \quad (3.4)$$

$$\frac{df_j}{dt} = \hat{e}_j \frac{\partial f_j}{\partial \omega_j} + \frac{1}{4} \hat{q}_j \nabla_{k_{\text{T}}}^2 f_j + \sum_i \int d\omega_i dk_{\text{T}i}^2 \frac{d\tilde{\Gamma}_{i \rightarrow j}}{d\omega_j dk_{\text{T}j}^2 dt} f_i - \sum_i \int d\omega_i dk_{\text{T}i}^2 \frac{d\tilde{\Gamma}_{j \rightarrow i}}{d\omega_i dk_{\text{T}i}^2 dt} f_i \quad (3.5)$$

448 where i is the type of parton, ω_i is its energy, and k_{T}^2 is its transverse momentum with respect to the jet axis.
 449 The first term in Equation 3.5 is the collisional energy loss, the second term is the transverse momentum
 450 broadening, and the last two terms are the medium induced gain and loss radiative processes respectively.
 451 The splitting processes are given by:

$$\frac{d\Gamma_{i \rightarrow j}}{d\omega_j dk_{\text{T}j}^2 dt} = \frac{2\alpha_S}{\pi} \hat{q}_g \frac{x P_{i \rightarrow j}(x)}{\omega_j k_{\text{T}j}^4} \sin^2 \left(\frac{t - t_i}{2\tau_f} \right) \quad (3.6)$$

452 where $P_{i \rightarrow j}$ is the vacuum splitting function for $i \rightarrow j$ with ω_j being the energy of the radiated parton, τ_f is
 453 the formation time of the radiated parton, and $k_{\text{T}j}$ is the transverse momentum of the radiated parton with
 454 respect to the parent parton. These transport Equations 3.5 can be solved numerically and agree with R_{AA}
 455 measurements [132, 134, 149]. The effects of the medium are included by considering the energy-momentum
 456 conservation of the jet-QGP system $\partial_\mu [T_{\text{QGP}}^{\mu\nu} + T_{\text{jet}}^{\mu\nu}] = 0$. Then the source term $J^\nu(x)$ that describes the
 457 energy transfer between the jet and the medium can be defined as $J^\nu(x) \equiv -\partial_\mu T_{\text{jet}}^{\mu\nu}$, making the QGP
 458 evolution being given by

$$\partial_\mu T_{\text{QGP}}^{\mu\nu} = j^\nu \quad (3.7)$$

which characterizes the energy-momentum transfer between the jet and the QGP.

An important component of this model is the flow induced by jets. This can be seen in Figure 3.3, where the evolution of the energy density of the medium can be seen in a sample event. A single jet travels through the QGP, and can be clearly seen in the lower panels after the energy of the medium has been subtracted out. The “V” shaped feature seen is the mach cone that is induced by the parton as it moves faster than the medium sound velocity.

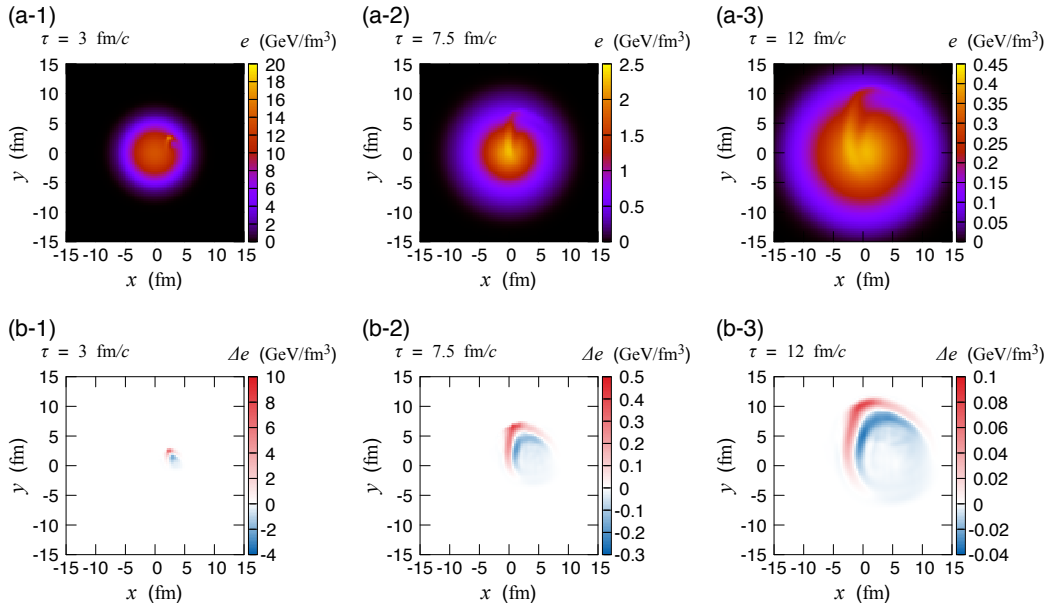


Figure 3.3: (Top) The time evolution of the energy density of the quark gluon plasma with a jet propagating through it. (Bottom) The time evolution of the energy density in the event after the energy density of the QGP has been subtracted out. Figure taken from [148].

The final jet energy has two components: the jet shower, and the hydrodynamic response. The former as discussed above comprises of the collisional energy loss, momentum broadening, and medium induced radiation. The latter includes the energy lost from the jet shower that thermalizes into the medium and induces conical flow, some of which is still in the jet cone. This compensates some of the energy lost in the shower and can be seen in Figure 3.4. While the absolute amount of energy lost increases as a function of initial jet energy, the fractional energy loss decreases. Furthermore there is a cone size dependence once the hydrodynamic contributions are included. This is a result of the jet being highly collimated, such that while

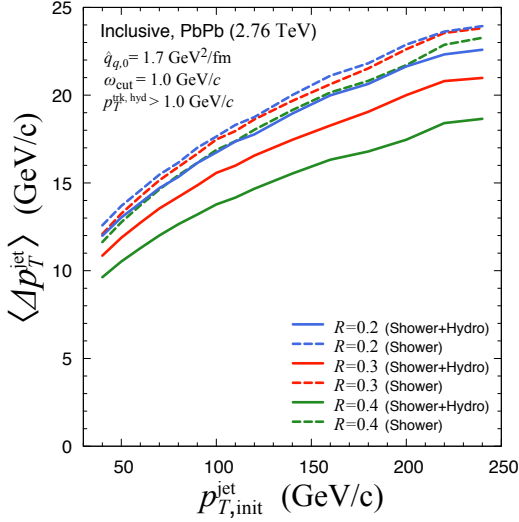


Figure 3.4: (Top) The energy lost by a jets of different radii as a function of their initial energy in central Pb+Pb collisions at $\sqrt{s_{\text{NN}}} = 2.76 \text{ TeV}$. Figure taken from [148].

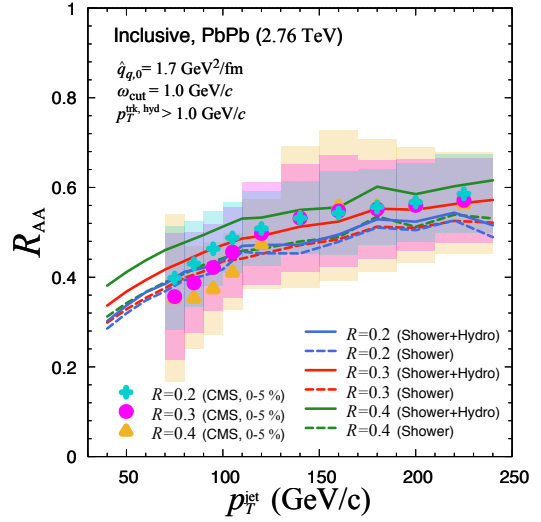


Figure 3.5: The jet R_{AA} measured by CMS [134] and compared to the Jet-Fluid model with and without the hydro dynamic contribution. Figure taken from [148].

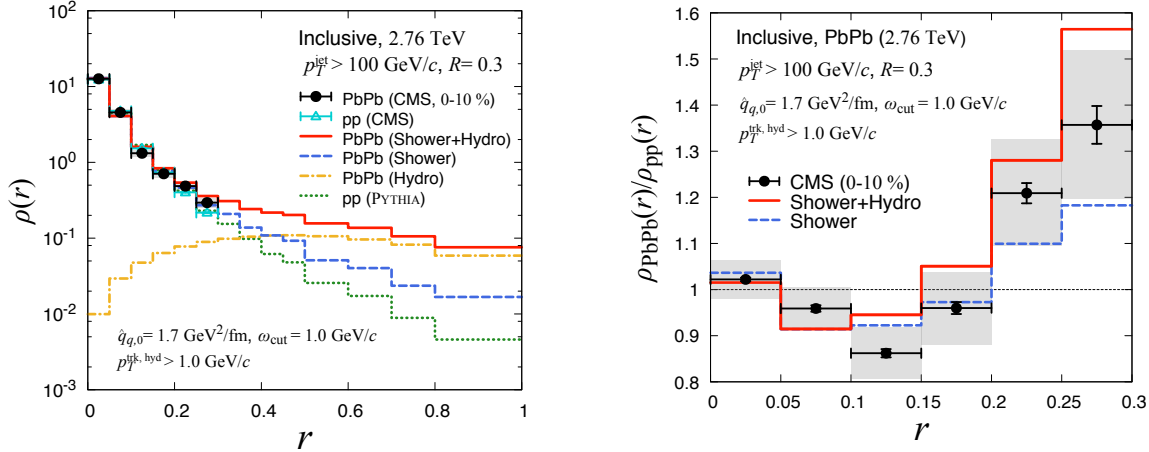
472 an increase in the size does not change the energy much, it does affect the hydrodynamic contribution from
 473 the medium.

474 The R_{AA} distributions constructed with this model and compared to data from CMS [134] are shown in
 475 Figure 3.5. Including the hydrodynamic contribution decreases the energy loss, hence increasing the R_{AA}
 476 value and inducing a cone size dependence to the R_{AA} .

477 The internal structure of the jet can be described using the jet shape variable, defined as a per-jet quantity
 478 as:

$$\rho_{\text{jet}} = \frac{1}{N_{\text{jet}}} \sum_{\text{jet}} \left[\frac{1}{p_{\text{T}}^{\text{jet}}} \frac{\sum_{\text{trk}} p_{\text{T}}^{\text{ch}}}{\delta r} \right] \quad (3.8)$$

479 where the sum is over all jets and for all tracks around a jet in an annulus with mean radius r from the jet axis.
 480 The modification in the jet structure then can be defined as $R_{\text{AA}}^{\rho} = \rho_{\text{AA}}(r)/\rho_{\text{pp}}(r)$. A comparison of the jet
 481 shape variable ρ and its modification R_{AA}^{ρ} to data measured by CMS is shown in Figure 3.6. The individual
 482 shower and hydro contributions are seen in Figure 3.6(a). These indicate that the shower contribution to the
 483 jet shape variable falls steeply as a function of distance from the jet axis while the hydro contribution is
 484 fairly constant at large distances. This is because the energy loss from the shower is carried away by the jet
 485 induced flow to large angles. The R_{AA}^{ρ} distribution in Figure 3.6(b), shows that the core is largely unmodified



(a) The jet shape as measured by CMS for pp and central $Pb+Pb$ collisions [150] compared to the Jet Fluid model. The shower (blue) and hydro (orange) contributions to the jet shape are highlighted.

(b) The modification of the jet shape between pp and $Pb+Pb$ as measured by CMS [150] and compared to the Jet Fluid model. The dashed line shows the modeled modification without the hydro-contribution.

Figure 3.6: Fits to CMS data. Figures taken from [148].

486 while the outer part of the jet is broadened. The hydro-contribution mainly has an effect at larger distances
 487 from the jet axis. This is consistent with the cone-size dependence seen in Figure 3.4.

488 3.3 Hybrid Model

489 This discussion is based on the work in Refs. [142, 151, 152] and describes jet quenching using a hybrid
 490 strong/weak model. It uses perturbative QCD to describe the weakly coupled hard process of jet production
 491 and holographic calculations of the energy loss of energetic probes to model the strong coupling between the
 492 probe and the plasma [153, 154]. This is a combination of approaches that focus on the following extreme
 493 limits: a weakly coupled system at unrealistically high temperatures that can be treated perturbatively
 494 [97, 155] and a system where the coupling constant is large at all energy scales and Gauge/string duality is
 495 applicable [156]. In this model, the jet evolves in space time with the lifetime of the parton in the shower
 496 being given by [157].

$$\tau = 2 \frac{E}{Q^2} \quad (3.9)$$

497 where Q is its virtuality and E its energy. This evolution is unaffected before the proper time at which the
 498 plasma hydrodynamizes, $\tau_{\text{hydro}} = 0.6$ fm. After this time, the jet-plasma interaction comes into play and the

499 fragments evolve with the energy loss as:

$$\frac{1}{E_{\text{in}}} \frac{dE}{dx} = -\frac{4}{\pi} \frac{x^2}{x_{\text{stop}}^2} \frac{1}{\sqrt{x_{\text{stop}}^2 - x^2}} \quad (3.10)$$

500 where E_{in} is the initial energy of the parton prior to any quenching and x_{stop} is its stopping distance (jet
501 thermalization distance). The stopping distance can be written as:

$$x_{\text{stop}} = \frac{1}{2\kappa_{\text{sc}}} \frac{E_{\text{in}}^{1/3}}{T^{4/3}} \quad (3.11)$$

502 where κ_{sc} is a dimensionless free parameter associated to the strong coupling and is used to fit to the data.

503 The energy loss is characterized by the strong x^2 dependence for $x \ll x_{\text{stop}}$. Furthermore, when x is
504 comparable to x_{stop} , dE/dx depends nontrivially on E_{in} and x , diverging for $x \rightarrow x_{\text{stop}}$ and $E \rightarrow 0$. The
505 shower is then embedded into a hydrodynamic description of the QGP from Ref. [158], and the energy loss
506 expressions are integrated for each parton, from the time it is produced to the time that it splits. The splitting
507 probabilities are taken to be independent of the medium, depending only on the initial energy of the daughter
508 partons. These further lose energy as they propagate through the QGP and split. Then the total energy
509 lost by a parton is dependent on the history of splitting and propagation of its parents, grandparents and so
510 on and so forth. The partons further experience kicks transverse to their direction of motion, a phenomena
511 called transverse momentum broadening. This effect is mainly experienced by softer partons that are much
512 more affected by the angular narrowing effects of energy loss, making most measured observables insensitive
513 to the size of this kick. This is directly related to wider jets losing more energy than narrower ones. The wake
514 left in the medium from the partons depositing momentum in the QGP as they propagate through it lends
515 a non-trivial impact to the model predictions. It is a vital part of any model since the contribution from
516 the wake is impossible to separate experimentally. This wake results in a perturbation to the hydrodynamic
517 background resulting in corrections to the final state hadron spectra, making it particularly important for jet
518 substructure observables like jet fragmentation and jet shapes [152].

519 A screening effect recently included in the hybrid model is based considering the resolving power of the
520 QGP [151]. As depicted in Figure 3.7, the QGP will only resolve daughter partons of a splitting after they
521 are separated by a certain distance L_{res} . It is only after they are resolved that they will be allowed them to
522 lose energy independent of each other. This delayed quenching results in an enhancement of softer partons at
523 larger angles from the jet axis compared to the case where the daughter partons are resolved immediately

524 after they split from the parent parton. The L_{res} parameter has the constraint $1/(\pi T) < L_{\text{res}} < 2/(p_{\text{T}}T)$
525 based on the Debye screening length for the plasma.

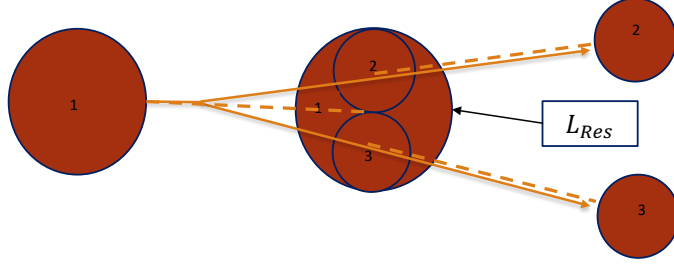


Figure 3.7: A schematic illustrating the resolving power of the QGP. The daughter partons 2 and 3 that come from 1 need to be separated by L_{res} before they are treated individually by the plasma. Prior to that separation, they are treated as one effective parton. Figure taken from [151].

526 The free parameter κ_{sc} is determined by fitting to jet R_{AA} data from CMS [134] as shown in Figure 3.8. It
527 can be seen that including the L_{res} parameter does not really affect the jet R_{AA} prediction. The dependence
528 of the R_{AA} on the size of the jet radius can be seen. This is consistent with the expectation that wider jets
529 lose more energy.

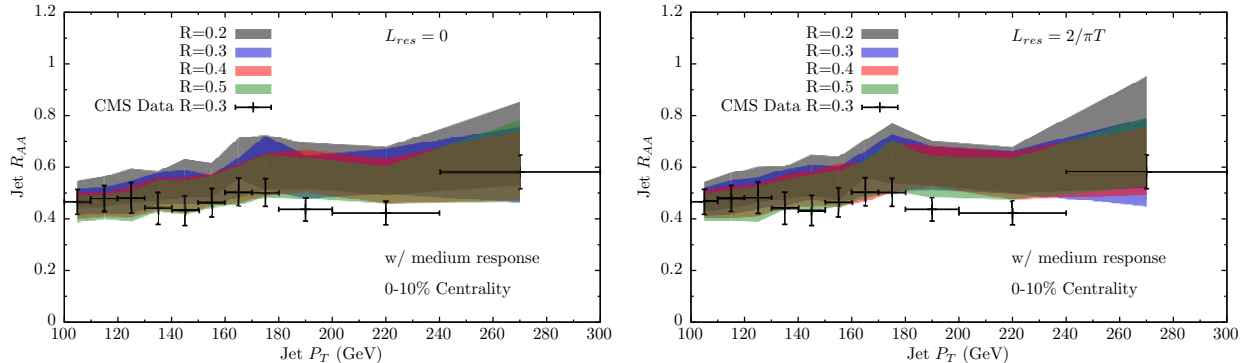
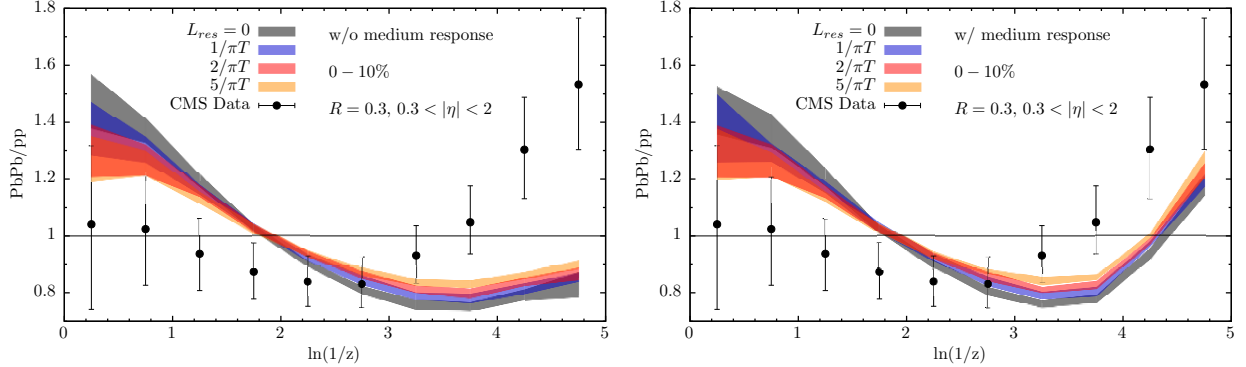


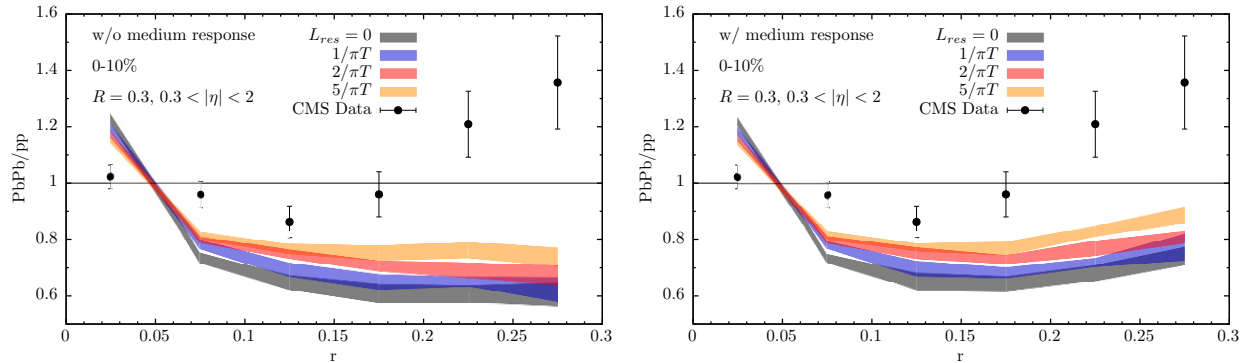
Figure 3.8: The hybrid model without (left) and with (right) the L_{res} parameter, compared to the jet R_{AA} as a function of jet p_{T} in two centrality intervals as measured in Ref. [134]. The different colors correspond to different jet radii. The Hybrid Model is fit to the 100–110 GeV point from the data, giving rise to the colored bands. Figure taken from [151].

530 Fixing the κ_{sc} parameter allows for predictions of other jet measurements like jet fragmentation and jet
531 shape. Figures 3.9(a) and 3.9(b) show a comparison of the measured and modeled values of the modifications
532 to the jet fragmentation and jet shape respectively. The model has also been compared to measurements
533 done by ATLAS, ALICE, and STAR [124, 149, 159]

534 Here it can be seen that adding a medium response and a non-zero L_{res} parameter affects the prediction.
535 While the hard fragments (see Figure 3.9(a)) are unaffected by the medium response, including the soft



(a) The modification to the jet fragmentation from pp to $Pb+Pb$ as a function of $\ln(1/z)$ as measured in Ref. [160] compared to the predictions of the hybrid model. The predictions are shown without (left) and with (right) the effect of the wake from the QGP responding to the jet. The different colors correspond to different L_{res} parameters. Figure taken from [151].



(b) The modification to the jet shape from pp to $Pb+Pb$ as a function of r as measured in Ref. [150] compared to the predictions of the hybrid model. The predictions are shown without (left) and with (right) the effect of the wake from the QGP responding to the jet. The different colors correspond to different L_{res} parameters. Figure taken from [151].

Figure 3.9: A comparison of measured data, MC, and the analytic calculation of the EQ model. Figure taken from [139]

536 particles from the wake compensates some of the suppression of soft fragments in Pb+Pb compared to pp
537 collisions. Moreover, including the L_{res} parameter further compensates the suppression for soft fragments,
538 while reducing the enhancement of the hard fragments. This is a result of allowing more hadrons carrying a
539 smaller fraction of the jet energy (low z , high ($\ln(1/z)$) to survive into the final state. The jet shape observable
540 (see Figure 3.9(b)) quantifies the radial distribution of energy in terms of annuli around the jet axis. It can
541 be seen that introducing the L_{res} parameter enhances the probability to find final state hadrons at larger
542 distances from the jet axis. The jet core ($r < 0.05$) is also affected, with the depletion only slowly evolving
543 with an increasing L_{res} . One must be careful before making conclusions though, since these modifications are
544 made between jets that are quenched (in Pb+Pb) and unquenched (in pp). Taking into account the fact
545 that wider jets lose more energy and that the jet spectrum rapidly falls off, there is a bias for finding narrower
546 quenched jets than unquenched jets. This makes the jet shape after quenching narrower in Pb+Pb compared
547 to pp . While the model is not fully able to capture the features in the data, including the medium response
548 moves it in the correct direction. It can be suggested that the model is missing a description of the medium
549 induced modification to the hadronization process or that the wakes in the plasma are not equilibrating.

Chapter 4

LHC and the ATLAS Detector

4.1 The Large Hadron Collider

550 The Large Hadron Collider (LHC) is a part of the European Organization for Nuclear Research (CERN).
551 It has a circumference of 27 kilometers, making it the world's largest particle accelerator, and is housed in
552 a tunnel that is up to 175 meters below the surface of the earth. The LHC ring has eight arcs and eight
553 straight sections, with each straight section being approximately 528 m long. Four of the straight sections
554 are where the major detectors are located, while the other four are used for machine utilities, radio frequency,
555 collimation and beam dumps. The arc sections are built using 1232 dipole superconducting magnets, providing
556 a magnetic field of up to 8.33 T. Another 392 quadrupole magnets are used for focussing the particle beam.
557 Sixteen radio frequency (RF) cavities that provide a voltage of 2 MV and operate at 400 MHz are used to
558 accelerate the proton or ion beams that are kept in their circular path by the dipole magnets. The magnets
559 are cooled down to 1.9 K via liquid Helium.
560

561 The LHC beam pipe has two rings with the counter-rotating beams and uses a twin-bore magnet
562 design that optimizes for both cost, as well as space. The counterrotating beams require opposite magnetic
563 dipole fields in both rings, with separate magnetic and vacuum chambers, with the common sections only
564 at the insertion regions and where the major experimental detectors are located. These detectors are: A
565 Toroidal LHC Apparatus (ATLAS), Compact Muon Solenoid (CMS), A Large Ion Collider Experiment
566 (ALICE), and Large Hadron Collider - Beauty (LHCb) [161].

567 Studying the rare events that the LHC was designed for requires high beam energies and intensities, and
568 the LHC is capable of reaching up to center of mass energies, $\sqrt{s} = 14$ TeV for protons and $\sqrt{s_{NN}} = 5.5$
569 TeV for lead ions. The LHC delivers up to $10^{34}\text{cm}^2\text{s}^{-1}$ of luminosity to the ATLAS and CMS detectors when
570 colliding protons. The LHCb detector is a lower luminosity experiment, that receives up to $10^{32}\text{cm}^2\text{s}^{-1}$, and
571 ALICE, a dedicated ion experiment aims at a peak luminosity of $10^{27}\text{cm}^2\text{s}^{-1}$ for nominal lead-lead operation.
572 In 2015, the LHC delivered an integrated luminosity of 0.49 pb^{-1} of Pb+Pb and 25 pb^{-1} of pp data.

573 A schematic of the entire accelerator complex and the path followed by protons and heavy ions is show

in Fig. 4.1. The protons in the LHC are obtained by stripping a hydrogen atom of its electrons with an electric field. They are then supplied to the LHC via the Linac2 - Proton Synchrotron Booster - Proton Synchrotron - Super Proton Synchrotron chain. The complete ionization of lead on the other hand is done in multiple stages, with the first stage in Linac3, which provides Pb^{+29} via an ion source. The Pb^{+29} lead ions are further stripped of electrons by passing them through a $0.3 \mu\text{m}$ foil. The Pb^{+54} ions are selected via mass spectrometer and sent to the Low Energy Ion Ring (LEIR), followed by the Proton Synchrotron and Super Proton Synchrotron, and then finally the LHC. The final stripping of lead ions takes place after the PS, on a 0.8 mm thin aluminum foil.

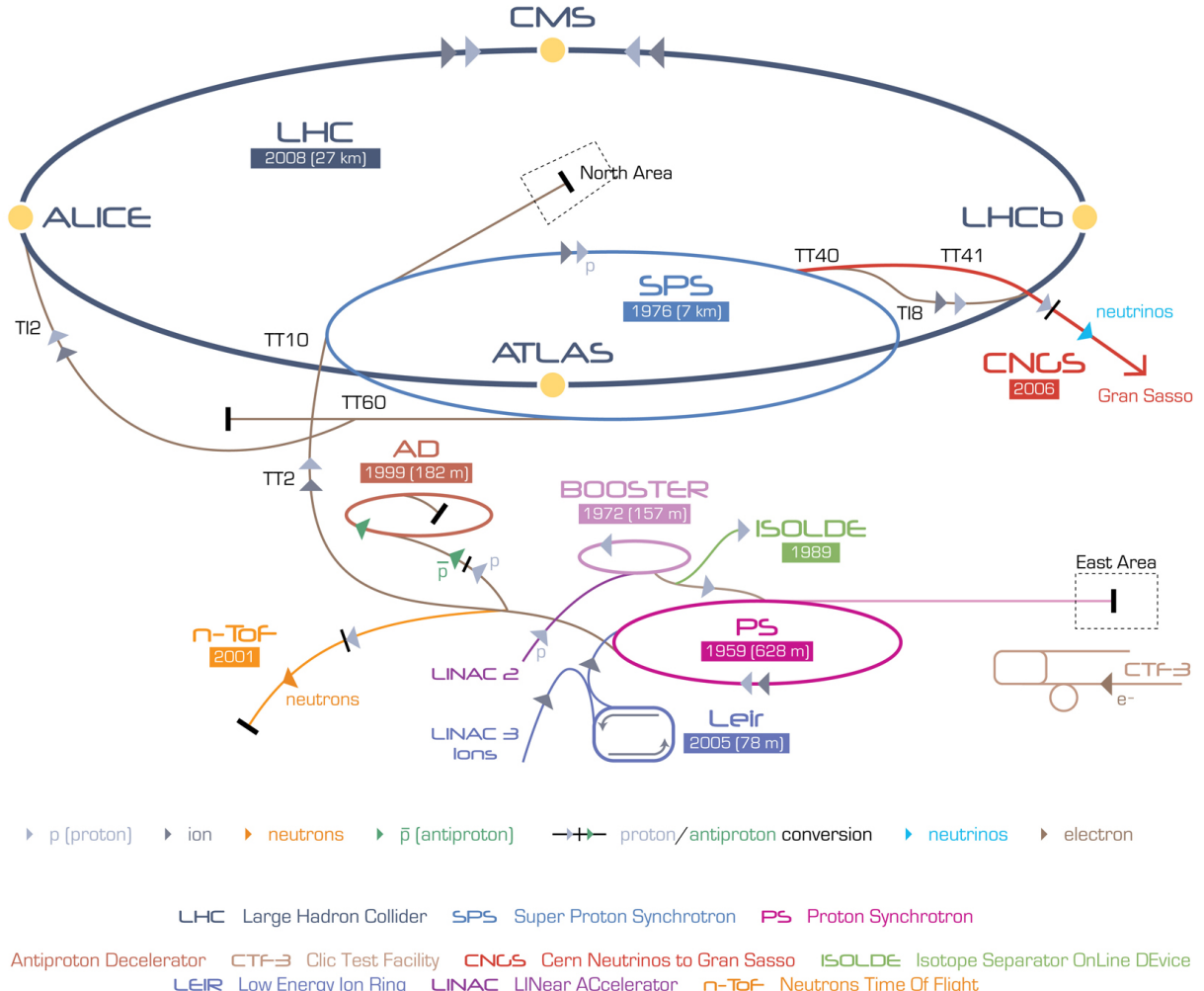


Figure 4.1: The accelerator complex at CERN. ATLAS can be seen inside the SPS on the LHC ring. Figure taken from Ref. [162].

582 4.2 The ATLAS Detector

583 The ATLAS detector (Fig. 4.2) is a general purpose detector at the LHC. It uses a right-handed coordinate
584 system with its origin at the nominal interaction point (IP) in the centre of the detector and the z -axis
585 along the beam pipe. The x -axis points from the IP to the centre of the LHC ring, and the y axis points
586 upward. Cylindrical coordinates (r, ϕ) are used in the transverse plane, ϕ being the azimuthal angle around
587 the beam pipe. The pseudorapidity is defined in terms of the polar angle θ as $\eta = -\ln \tan(\theta/2)$. The detector
588 is symmetric in the forward-backward direction, with the positive z direction being the A side, and the
589 negative z direction being the C side. It has full 2π coverage in azimuth. The transverse momentum p_T , the
590 transverse energy E_T , and the missing transverse energy $E_{T\text{miss}}$ are defined in the $x - y$ plane unless stated
591 otherwise. The distance ΔR in the pseudorapidity-azimuthal angle space is defined as $\Delta R = \sqrt{\Delta\eta^2 + \Delta\phi^2}$.

592 The detector was designed keeping in mind the goals of the physics it aimed to explore, and as such has
593 the following characteristics:

- 594 • Fast, radiation-hard electronics and sensor
- 595 • Fine granularity to be able to manage large particle fluxes
- 596 • Large acceptance in pseudorapidity and full azimuthal coverage
- 597 • Good electromagnetic calorimetry for photon and electron identification
- 598 • Good hadron calorimetry for accurate jet and missing transverse energy measurements
- 599 • Good muon identification and momentum resolution
- 600 • Highly efficient trigger system

601 These design goals are achieved with the main subsystems: the inner detector, the calorimeter, the muon
602 spectrometer, and the trigger system. The main analysis discussed in this thesis uses the inner detector,
603 calorimeter, and the trigger system. The muon system is described for completeness.

604 4.2.1 Inner Detector

605 The inner detector shown in Figure 4.3 is designed to reconstruct the charged particle trajectories for particles
606 with momenta down to 0.5 GeV in the interval $|\eta| < 2.5$. It is immersed in a 2T magnetic field from the
607 central solenoid that covers a region of 5.3 m long and has a diameter of 2.5 m. The inner detector has
608 capabilities for pattern recognition, momentum and vertex measurements, and electron identification. These

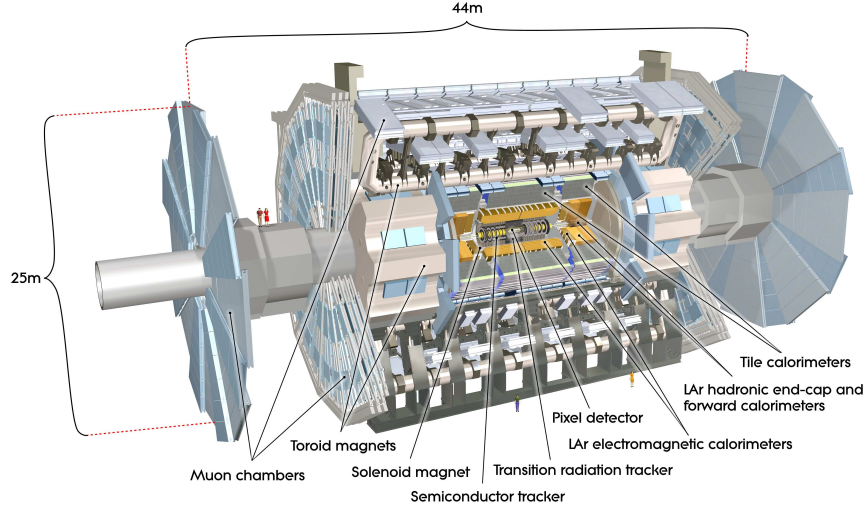


Figure 4.2: The ATLAS detector. Figure taken from Ref. [163].

609 measurements are made using the inner pixel detector, the semi-conductor tracker (SCT), and the transition
 610 radiation tracker (TRT).

611 **Pixel system:** This system is segmented in $R - \phi$ and comprises of four pixel layers : the innermost
 612 insertable B layer (IBL) and three identical silicon pixel detectors. The IBL was added to the ATLAS detector
 613 during the first long shutdown of the LHC in 2013-2014. It consists of 14 carbon fiber staves, 2 cm wide and
 614 64 cm long, surrounding the beam pipe at a mean radius of 33 mm, and covering a pseudorapidity region of
 615 ± 3 . Each stave consists of 26880 pixels in a matrix of 80 columns ($50 \mu\text{m}$ pitch), by 336 rows ($250 \mu\text{m}$ pitch)
 616 [164, 165]. The other three layers have a pixel size in $R - \phi \times z$ of $50 \times 400 \mu\text{m}^2$. The accuracies in the
 617 barrel region are $10 \mu\text{m}^2$ ($R - \phi$) and $115 \mu\text{m}^2$ (z). The end cap regions have an accuracy of $10 \mu\text{m}^2$ ($R - \phi$)
 618 and $115 \mu\text{m}^2$ (R). The hit resolution ranges from ~ 8 ($R - \phi$) and $\sim 40 \mu\text{m}$ (z) for the innermost layer, to \sim
 619 $10 \mu\text{m}$ ($R - \phi$) and $\sim 115 \mu\text{m}$ (z) for the next three layers [163]. The pixel detector has approximately 80.4
 620 million readout channels.

621 **Semi Conductor Tracker:** This subsystem has a coverage that overlaps with the pixel layers, and
 622 is arranged in concentric cylinders around the beam axis, with the end caps being disks perpendicular to
 623 the beam axis. The SCT has eight strip ($80 \mu\text{m}$ pitch) layers that are crossed by each track. Small angle
 624 stereo strips (40 mrad) are used to measure both coordinates, with one set of strips in each layer, parallel to
 625 the beam direction. The end cap region has nine layers of double sided modules with strips in the radial
 626 direction, with each also having a mean pitch of $80 \mu\text{m}$. The intrinsic resolution is $\sim 17 \mu\text{m}$ ($R - \phi$) and \sim
 627 $580 \mu\text{m}$ (z). There are approximately 6.3 million readout channels from the SCT [163].

628 **Transition Radiation Tracker:** The TRT uses a combination of a xenon based gas and 4mm diameter
 629 straw tubes and provides for a large number of hits (up to 36) per track. It covers the region $|\eta| < 2.0$, and
 630 has a resolution of $\sim 130\mu\text{m}$ in $r - \phi$, with no information in the z direction. The barrel region of the TRT
 631 has straws that are 144 cm long and are parallel to the beam axis, with the wires divided into two halves at
 632 $\eta = 0$. The end-caps have 37 cm long straws in a radial configuration. The TRT has approximately 315,000
 633 channels [163].

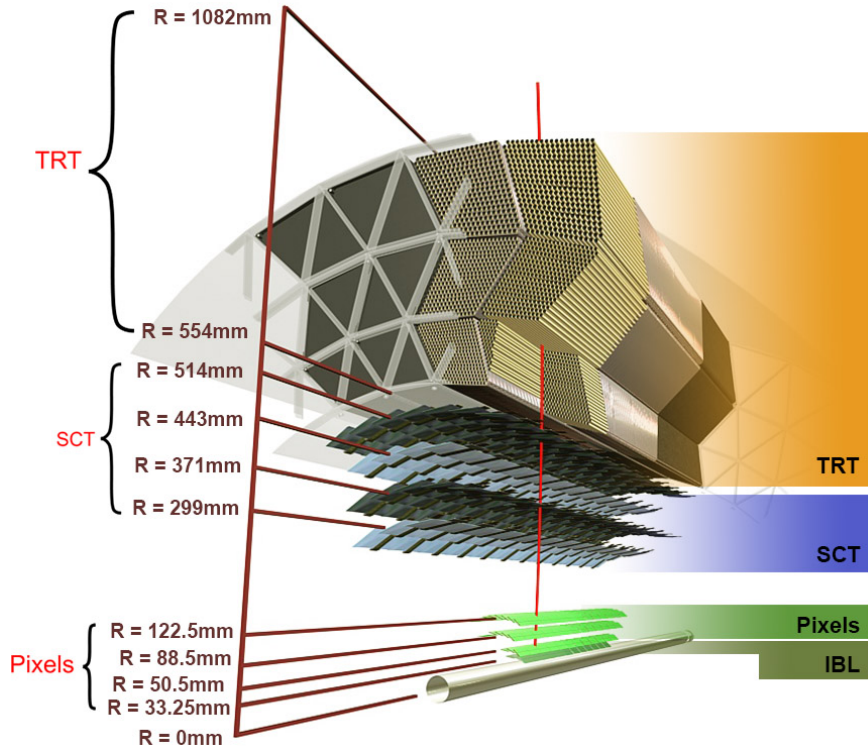


Figure 4.3: ATLAS Inner Detector System. Figure taken from Ref. [166].

634 4.2.2 Calorimeter

635 The calorimeter covers the range of $|\eta| < 4.9$ for using a variety of different techniques. The parameters are
 636 summarized in the table below. Over $|\eta| < 2.5$, where there is overlap with the inner detector, the highly
 637 granular electromagnetic calorimeter is used for precision measurements of electrons and photons. The rest
 638 of calorimeter has coarser granularity that is sufficient for jet reconstruction. The calorimeter contains the
 639 electromagnetic and hadronic showers, and limits the punch through to the muon system. The EMCAL has a
 640 radiation depth greater than 22 radiation lengths in the barrel, and greater than 24 radiation lengths in the
 641 end caps. The approximately 10 interaction lengths in the barrel and end cap provide good resolution for
 642 high energy jets. The total thickness of the calorimeter is 11 interaction lengths at $\eta = 0$. The calorimeter is

643 divided into different subsystems, including the Liquid Argon Electromagnetic Calorimeter (LAr EMCal)
644 and the Hadronic calorimeter (HCal).

645 **LAr EMCal:** The EMCal covers the region $|\eta| < 1.475$ and has two end caps ($1.375 < |\eta| < 3.2$). It
646 also contains the central solenoid. The barrel calorimeter is divided into two half barrels, separated by 4mm
647 at $z = 0$. Each end cap is divided into two coaxial wheels, with the inner one covering $2.5 < |\eta| < 3.2$ and the
648 outer one covering $1.375 < |\eta| < 2.5$. The EMCal uses accordion shaped kapton electrodes and lead absorber
649 plates that provide full azimuthal symmetry. The EMCal is subdivided into three sections in its depth over
650 $|\eta| < 2.5$, the region used for precision physics. The $|\eta| < 1.8$ region also uses a pre-sampler detector that
651 uses an active LAr layer to correct for energy lost upstream of the calorimeter. A main source of this loss is
652 the central solenoid.

653 **Hadronic Calorimeter:** The hadronic calorimeter consists of the tile, LAr Hadronic end cap, and
654 the LAr forward calorimeter. The tile covers the region $|\eta| < 1.0$, with its two barrels covering the range eta
655 $0.8 < |\eta| < 1.7$. It uses steel as the absorber and scintillating tiles for the active material. The tile calorimeter
656 extends radially from an inner radius of 2.28 m to 4.25 m. It has a three layer that are 1.5, 4.1, and 1.8
657 interaction lengths thick in the barrel region, and 1.5, 2.6, and 3.3 interaction lengths in the extended barrel
658 region. The total detector thickness is 9.7 interaction lengths at $\eta = 0$.

659 The LAr hadronic end cap calorimeter (HEC) consists of two independent wheels per end cap, and is
660 behind the EMCal end cap. It extends out from $1.5 < |\eta| < 3.2$, and overlaps with the forward calorimeter
661 and the tile calorimeter. The HEC covers the radial region of 0.475 to 2.03 m.

662 The LAr Forward calorimeter provides coverage over the $3.1 < |\eta| < 4.9$. It is approximately 10 interaction
663 lengths deep, and has three modules, one of which is optimized for electromagnetic measurements, while the
664 other two for hadronic measurements. Each module is made of concentric rods and tubes parallel to the
665 beam axis.

666 A summary of the depth of the calorimeter in terms of the interaction lengths, as a function of pseu-
667 dorapidity is shown in Fig. 4.4.

668 4.2.3 Muon Spectrometer

669 The muon spectrometer is based on the magnetic deflection of muon tracks in the toroid magnets. The
670 barrel toroid provides bending over the $|\eta| < 1.4$ range, and the end cap magnets provide bending in the
671 $1.6 < |\eta| < 2.7$ range. In the transition region ($1.4 < |\eta| < 1.6$), the magnetic deflection is from a combination
672 of the barrel and end-cap fields. The barrel region has tracks that are measured in chambers in a cylindrical

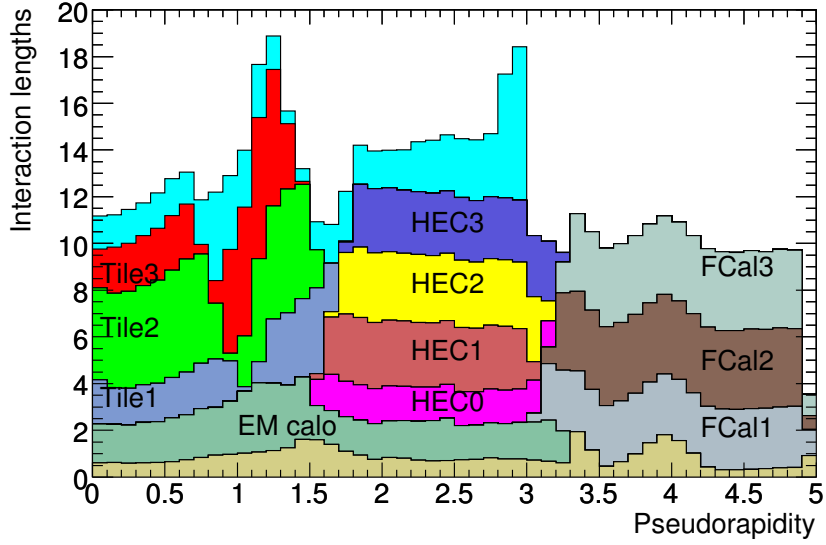


Figure 4.4: Cumulative material in the calorimeter system in units of hadronic interaction length as a function of $|\eta|$. Figure taken from Ref. [163].

673 configuration around the beam axis. The transition and end-cap have chambers perpendicular to the beam
674 axis.

675 4.2.4 Other subsystems

676 Other major subsystems of the ATLAS detector include the Zero Degree Calorimeter (ZDC), the trigger
677 system

678 ZDC

679 The zero degree calorimeter plays a key role in determining the centrality of heavy ion collisions. It consists of
680 quartz rods and tungsten plates, and measures neutral particles at $|\eta| \geq 8.2$. It is made of four modules, one
681 electromagnetic, and three hadronic. The Modules are made of 11 tungsten plates that are perpendicular to
682 the beam direction. Photomultiplier tubes are used to detect the Cherenkov radiation from particle showers.

683 Trigger System

684 The trigger and data acquisition system (TDAQ) have different subsystems that are associated with sub-
685 detectors. There are three distinct levels: L1, L2, and the event filter. The latter two form the High Level
686 Trigger (HLT) system. The L1 trigger uses custom electronics, while the HLT is software based. Each level
687 uses information from the previous level to select events. The first level uses limited detector information and

688 makes decisions based on muons, electron, photons, jets, and τ -leptons carrying a high transverse momentum.
 689 It is also capable of identifying large missing and total transverse energy. It has a maximum acceptance rate
 690 of 75kHz and makes a decision in less than $2.5\mu\text{s}$. This event rate is further reduced to 200 Hz by the HLT
 691 that uses the full granularity and precision of the inner detector, calorimeter and muon systems to select
 692 events.

693 4.3 Jet Reconstruction for Heavy Ion Collisions in ATLAS

694 The ATLAS jet reconstruction procedure is summarized in Figure 4.5. For heavy ion collisions in ATLAS,
 695 the inputs to the algorithm are the $\eta \times \phi = 0.1 \times 0.1$ calorimeter towers. The tower energies are determined
 696 by summing up the energies of the individual calorimeter cells. The anti- k_t algorithm is first run with the
 697 distance parameter $R = 0.2$, following which an underlying event subtraction procedure is performed. A first
 698 estimate of the average underlying event energy density $\rho_i(\eta)$ is done in 0.1 slices of η in each calorimeter
 699 layer i after excluding the regions that overlap with the seed jets. A modulation of $2v_2 \cos[2(\phi - \Psi_2)]$ is
 700 applied to account for the flow from the QGP and the underlying event is subtracted to give E_{Tj}^{sub} :

$$E_{Tj}^{\text{sub}} = E_{Tj} - A_j \rho_i(\eta_j) \left(1 + 2 \sum_{n=2}^4 v_{ni} (\cos[2(\phi - \Psi_n)]) \right) \quad (4.1)$$

701 where E_{Tj} , η_j , ϕ_j and A_j are the cell E_T , η , ϕ and area for cell j in layer i . This process is done iteratively
 702 done one more time after getting new seeds with the distance parameter $R = 0.2$ and excluding areas that
 703 are within $\Delta R = 0.4$ of the seeds. Updated values of ρ'_i and v'_2 are recalculated and used to estimate the
 704 background that is subtracted from the original cell energies. More details on this procedure can be found in
 705 [124].

706 The η coverage of the different detector systems can be seen in Fig. ??.

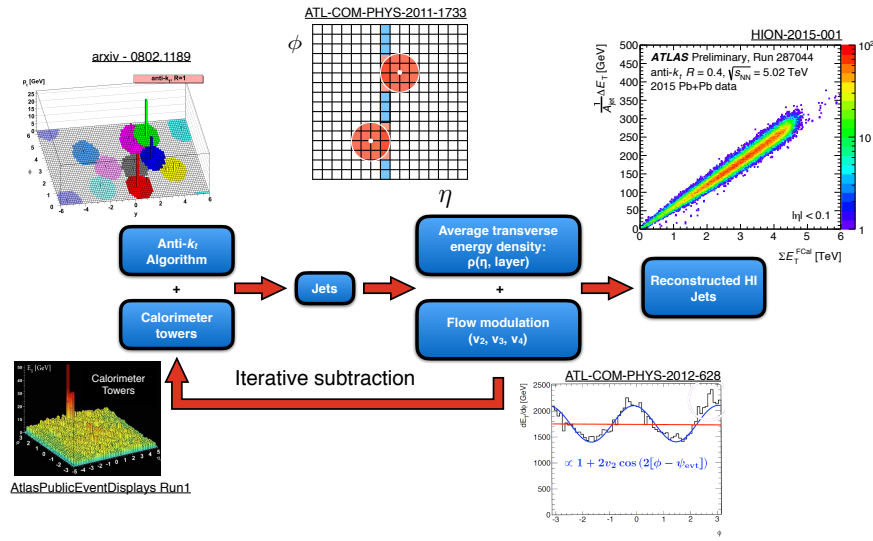


Figure 4.5: A schematic of the ATLAS jet reconstruction procedure. Figures taken from [1].

Bibliography

- 707 [1] M. K. Gaillard, P. D. Grannis and F. J. Sciulli, *The Standard model of particle physics*, Rev. Mod.
708 Phys. **71** (1999) S96, arXiv: [hep-ph/9812285 \[hep-ph\]](#) (cit. on p. 1).
- 709 [2] Wikimedia Commons, *Standard Model of Elementary Particles*, (2006), URL: https://en.wikipedia.org/wiki/Standard_Model (cit. on p. 1).
- 711 [3] J Beringer et al., *Review of Particle Physics, 2012-2013. Review of Particle Properties*, Phys. Rev. D
712 **86** (2012) 010001 (cit. on pp. 2, 3).
- 713 [4] D. J. Gross and F. Wilczek, *Ultraviolet Behavior of Non-Abelian Gauge Theories*, Phys. Rev. Lett. **30**
714 (26 1973) 1343, URL: <https://link.aps.org/doi/10.1103/PhysRevLett.30.1343> (cit. on p. 3).
- 715 [5] D. J. Gross and F. Wilczek, *Asymptotically Free Gauge Theories. I*, Phys. Rev. D **8** (10 1973) 3633,
716 URL: <https://link.aps.org/doi/10.1103/PhysRevD.8.3633> (cit. on p. 3).
- 717 [6] A. Deur et al., *High precision determination of the Q^2 evolution of the Bjorken Sum*, Phys. Rev. **D90**
718 (2014) 012009, arXiv: [1405.7854 \[nucl-ex\]](#) (cit. on p. 4).
- 719 [7] J. H. Kim et al., *A Measurement of $\alpha_s(Q^2)$ from the Gross-Llewellyn Smith sum rule*, Phys. Rev. Lett.
720 **81** (1998) 3595, arXiv: [hep-ex/9808015 \[hep-ex\]](#) (cit. on p. 4).
- 721 [8] G. Altarelli et al., *Determination of the Bjorken sum and strong coupling from polarized structure
722 functions*, Nucl. Phys. **B496** (1997) 337, arXiv: [hep-ph/9701289 \[hep-ph\]](#) (cit. on p. 4).
- 723 [9] H. W. Kendall, *Deep inelastic scattering: Experiments on the proton and the observation of scaling*,
724 Rev. Mod. Phys. **63** (3 1991) 597 (cit. on p. 4).
- 725 [10] A. L. Kataev, G. Parente and A. V. Sidorov, *Improved fits to the xF_3 CCFR data at the next-to-next-to-
726 leading order and beyond*, Phys. Part. Nucl. **34** (2003) 20, [Erratum: Phys. Part. Nucl.38,no.6,827(2007)],
727 arXiv: [hep-ph/0106221 \[hep-ph\]](#) (cit. on p. 4).
- 728 [11] S. Alekhin, J. Blumlein and S. Moch, *Parton Distribution Functions and Benchmark Cross Sections
729 at NNLO*, Phys. Rev. **D86** (2012) 054009, arXiv: [1202.2281 \[hep-ph\]](#) (cit. on p. 4).

- [12] S. Alekhin, J. Blumlein and S.-O. Moch, *ABM news and benchmarks*, PoS **DIS2013** (2013) 039, arXiv: 1308.5166 [hep-ph] (cit. on p. 4).
- [13] J. Blumlein, H. Bottcher and A. Guffanti, *Non-singlet QCD analysis of deep inelastic world data at $O(\alpha_s^3)$* , Nucl. Phys. **B774** (2007) 182, arXiv: hep-ph/0607200 [hep-ph] (cit. on p. 4).
- [14] H1 Collaboration, *Three- and Four-jet Production at Low x at HERA*, Eur. Phys. J. **C54** (2008) 389, arXiv: 0711.2606 [hep-ex] (cit. on p. 4).
- [15] ZEUS Collaboration, *Forward-jet production in deep inelastic ep scattering at HERA*, Eur. Phys. J. **C52** (2007) 515, arXiv: 0707.3093 [hep-ex] (cit. on p. 4).
- [16] ZEUS Collaboration, *Multi-jet cross-sections in charged current $e^\pm p$ scattering at HERA*, Phys. Rev. **D78** (2008) 032004, arXiv: 0802.3955 [hep-ex] (cit. on p. 4).
- [17] ZEUS Collaboration, *Inclusive dijet cross sections in neutral current deep inelastic scattering at HERA*, Eur. Phys. J. **C70** (2010) 965, arXiv: 1010.6167 [hep-ex] (cit. on p. 4).
- [18] ZEUS Collaboration, *Inclusive-jet cross sections in NC DIS at HERA and a comparison of the kT , anti- kT and SIScone jet algorithms*, Phys. Lett. **B691** (2010) 127, arXiv: 1003.2923 [hep-ex] (cit. on p. 4).
- [19] H1 Collaboration, *Jet Production in ep Collisions at High Q^2 and Determination of α_s* , Eur. Phys. J. **C65** (2010) 363, arXiv: 0904.3870 [hep-ex] (cit. on p. 4).
- [20] E. D. Bloom et al., *High-Energy Inelastic $e - p$ Scattering at 6° and 10°* , Phys. Rev. Lett. **23** (16 1969) 930, URL: <https://link.aps.org/doi/10.1103/PhysRevLett.23.930> (cit. on p. 4).
- [21] M. Breidenbach et al., *Observed Behavior of Highly Inelastic Electron-Proton Scattering*, Phys. Rev. Lett. **23** (16 1969) 935, URL: <https://link.aps.org/doi/10.1103/PhysRevLett.23.935> (cit. on p. 4).
- [22] J. D. Bjorken, *Asymptotic Sum Rules at Infinite Momentum*, Phys. Rev. **179** (5 1969) 1547, URL: <https://link.aps.org/doi/10.1103/PhysRev.179.1547> (cit. on p. 4).
- [23] K. Nishijima, *BRS invariance, asymptotic freedom and color confinement (a review)*, Czechoslovak Journal of Physics **46** (1996) 1, ISSN: 1572-9486, URL: <https://doi.org/10.1007/BF01692238> (cit. on p. 4).
- [24] K. G. Wilson, *Confinement of quarks*, Phys. Rev. D **10** (8 1974) 2445, URL: <https://link.aps.org/doi/10.1103/PhysRevD.10.2445> (cit. on p. 4).

- 759 [25] W. Buchmuller, *Fine- and hyperfine structure of quarkonia*, Physics Letters B **112** (1982) 479 ,
760 ISSN: 0370-2693, URL: <http://www.sciencedirect.com/science/article/pii/0370269382908541>
761 (cit. on p. 4).
- 762 [26] J. Kogut, D. Sinclair and L. Susskind, *A quantitative approach to low-energy quantum chromodynamics*,
763 Nuclear Physics B **114** (1976) 199 , ISSN: 0550-3213, URL: <http://www.sciencedirect.com/science/article/pii/0550321376905861> (cit. on p. 4).
- 764 [27] N. Isgur and J. Paton, *Flux-tube model for hadrons in QCD*, Phys. Rev. D **31** (11 1985) 2910, URL:
765 <https://link.aps.org/doi/10.1103/PhysRevD.31.2910> (cit. on p. 4).
- 766 [28] M. Faber, J. Greensite and Olejnks, *Casimir scaling from center vortices: Towards an understanding
767 of the adjoint string tension*, Phys. Rev. D **57** (4 1998) 2603, URL: <https://link.aps.org/doi/10.1103/PhysRevD.57.2603> (cit. on p. 4).
- 768 [29] G. S. Bali, *Casimir scaling of SU(3) static potentials*, Phys. Rev. D **62** (11 2000) 114503, URL:
769 <https://link.aps.org/doi/10.1103/PhysRevD.62.114503> (cit. on p. 4).
- 770 [30] J. B. Kogut, *The lattice gauge theory approach to quantum chromodynamics*, Rev. Mod. Phys. **55** (3
771 1983) 775, URL: <https://link.aps.org/doi/10.1103/RevModPhys.55.775> (cit. on p. 4).
- 772 [31] D. Zwanziger, *No Confinement without Coulomb Confinement*, Phys. Rev. Lett. **90** (10 2003) 102001,
773 URL: <https://link.aps.org/doi/10.1103/PhysRevLett.90.102001> (cit. on p. 4).
- 774 [32] A. Jaffe and E. Witten, *Yang-Mills and Mass Gap*, <http://www.claymath.org/millennium-problems/yang-mills-and-mass-gap> (cit. on p. 4).
- 775 [33] E. V. Shuryak, *Quantum chromodynamics and the theory of superdense matter*, Physics Reports **61**
776 (1980) 71 , ISSN: 0370-1573 (cit. on pp. 4, 8).
- 777 [34] J. C. Collins and M. J. Perry, *Superdense Matter: Neutrons or Asymptotically Free Quarks?*, Phys.
778 Rev. Lett. **34** (21 1975) 1353 (cit. on pp. 4, 5).
- 779 [35] A. D. Linde, *Phase transitions in gauge theories and cosmology*, Reports on Progress in Physics **42**
780 (1979) 389 (cit. on p. 4).
- 781 [36] LIGO/VIRGO Collaboration, *GW170817: Observation of Gravitational Waves from a Binary Neutron
782 Star Inspiral*, Phys. Rev. Lett. **119** (16 2017) 161101, URL: <https://link.aps.org/doi/10.1103/PhysRevLett.119.161101> (cit. on p. 4).
- 783 [37] S. Han and A. W. Steiner, *Tidal deformability with sharp phase transitions in (binary) neutron stars*,
784 Phys. Rev. **D99** (2019) 083014, arXiv: [1810.10967 \[nucl-th\]](https://arxiv.org/abs/1810.10967) (cit. on p. 4).
- 785
- 786
- 787
- 788

- 789 [38] J.-E. Christian, A. Zacchi and J. Schaffner-Bielich, *Signals in the tidal deformability for phase*
 790 *transitions in compact stars with constraints from GW170817*, Phys. Rev. D **99** (2 2019) 023009, URL:
 791 <https://link.aps.org/doi/10.1103/PhysRevD.99.023009> (cit. on p. 4).
- 792 [39] E. R. Most et al., *Signatures of Quark-Hadron Phase Transitions in General-Relativistic Neutron-Star*
 793 *Mergers*, Phys. Rev. Lett. **122** (6 2019) 061101, URL: <https://link.aps.org/doi/10.1103/PhysRevLett.122.061101> (cit. on p. 4).
- 795 [40] A. Bauswein, H.-T. Janka, K. Hebeler and A. Schwenk, *Equation-of-state dependence of the gravitational-*
 796 *wave signal from the ring-down phase of neutron-star mergers*, Phys. Rev. D **86** (6 2012) 063001, URL:
 797 <https://link.aps.org/doi/10.1103/PhysRevD.86.063001> (cit. on p. 4).
- 798 [41] A. Bauswein et al., *Identifying a First-Order Phase Transition in Neutron-Star Mergers through*
 799 *Gravitational Waves*, Phys. Rev. Lett. **122** (6 2019) 061102, URL: <https://link.aps.org/doi/10.1103/PhysRevLett.122.061102> (cit. on p. 5).
- 801 [42] S. Borsanyi et al., *Is there still any T_c mystery in lattice QCD? Results with physical masses in the*
 802 *continuum limit III*, JHEP **09** (2010) 073, arXiv: [1005.3508 \[hep-lat\]](https://arxiv.org/abs/1005.3508) (cit. on p. 5).
- 803 [43] A. S. Kronfeld, *Twenty-first Century Lattice Gauge Theory: Results from the QCD Lagrangian*, Ann.
 804 Rev. Nucl. Part. Sci. **62** (2012) 265, arXiv: [1203.1204 \[hep-lat\]](https://arxiv.org/abs/1203.1204) (cit. on p. 5).
- 805 [44] J. W. Harris and B. Muller, *The search for the quark-gluon plasma*, Annual Review of Nuclear and
 806 Particle Science **46** (1996) 71, eprint: <https://doi.org/10.1146/annurev.nucl.46.1.71>, URL:
 807 <https://doi.org/10.1146/annurev.nucl.46.1.71> (cit. on p. 5).
- 808 [45] PHENIX Collaboration, *Enhanced Production of Direct Photons in Au + Au Collisions at $\sqrt{s_{NN}} =$*
 809 *200 GeV and Implications for the Initial Temperature*, Phys. Rev. Lett. **104** (13 2010) 132301 (cit. on
 810 p. 5).
- 811 [46] ALICE Collaboration, *Direct photon production in Pb–Pb collisions at $s_{NN}=2.76$ TeV*, Physics Letters
 812 B **754** (2016) 235 , ISSN: 0370-2693 (cit. on p. 5).
- 813 [47] Z. Fodor and S. Katz, *Critical point of QCD at finite T and λ , lattice results for physical quark masses*,
 814 Journal of High Energy Physics **2004** (2004) 050 (cit. on p. 5).
- 815 [48] STAR Collaboration, *Experimental and theoretical challenges in the search for the quark-gluon plasma: The STAR Collaboration's critical assessment of the evidence from RHIC collisions*, Nuclear Physics
 816 A **757** (2005) 102 , First Three Years of Operation of RHIC, ISSN: 0375-9474 (cit. on p. 5).
- 818 [49] ALICE Collaboration, *Production of light nuclei and anti-nuclei in pp and Pb-Pb collisions at energies available at the CERN Large Hadron Collider*, Phys. Rev. C **93** (2 2016) 024917 (cit. on p. 5).

- 820 [50] PHENIX Collaboration, *Single identified hadron spectra from $\sqrt{s_{NN}} = 130$ GeV Au + Au collisions*,
 821 *Phys. Rev. C* **69** (2 2004) 024904 (cit. on p. 5).
- 822 [51] BRAHMS Collaboration, *Centrality dependent particle production at $y = 0$ and $y \geq 1$ in Au+Au collisions*
 823 *at $\sqrt{s_{NN}} = 200$ GeV*, *Phys. Rev. C* **72** (1 2005) 014908 (cit. on p. 5).
- 824 [52] PHOBOS Collaboration, *Identified hadron transverse momentum spectra in Au+Au collisions at*
 825 *$\sqrt{s_{NN}} = 62.4$ GeV*, *Phys. Rev. C* **75** (2 2007) 024910 (cit. on p. 5).
- 826 [53] ALICE Collaboration, *Centrality dependence of π , K , and p production in Pb-Pb collisions at $\sqrt{s_{NN}} =$*
 827 *2.76 TeV*, *Phys. Rev. C* **88** (4 2013) 044910 (cit. on p. 5).
- 828 [54] U. Heinz and R. Snellings, *Collective flow and viscosity in relativistic heavy-ion collisions*, Annual
 829 Review of Nuclear and Particle Science **63** (2013) 123 (cit. on p. 5).
- 830 [55] M. Gyulassy, ‘The QGP Discovered at RHIC’, *Structure and Dynamics of Elementary Matter*, ed.
 831 by W. Greiner, M. G. Itkis, J. Reinhardt and M. C. Gucu, Springer Netherlands, 2004 159, ISBN:
 832 978-1-4020-2705-5 (cit. on p. 5).
- 833 [56] W. Busza et al., *Heavy Ion Collisions: The Big Picture, and the Big Questions*, *Ann. Rev. Nucl. Part.*
 834 *Sci.* **68** (2018) 339, arXiv: [1802.04801 \[hep-ph\]](#) (cit. on pp. 6–8).
- 835 [57] A. Ster, T. Csorgo and B. Lorstad, *The Reconstructed final state of Pb + Pb 158-GeV/A reactions*
 836 *from spectra and correlation data of NA49, NA44 and WA98*, *Nucl. Phys.* **A661** (1999) 419, arXiv:
 837 [hep-ph/9907338 \[hep-ph\]](#) (cit. on p. 6).
- 838 [58] A. M. Poskanzer et al., *Centrality dependence of directed and elliptic flow at the SPS*, *Nucl. Phys.*
 839 *A661* (1999) 341, arXiv: [nucl-ex/9906013 \[nucl-ex\]](#) (cit. on p. 6).
- 840 [59] C. Pinkenburg et al., *Elliptic flow: Transition from out-of-plane to in-plane emission in Au + Au*
 841 *collisions*, *Phys. Rev. Lett.* **83** (1999) 1295, arXiv: [nucl-ex/9903010 \[nucl-ex\]](#) (cit. on p. 6).
- 842 [60] ATLAS Collaboration, *Measurement of the azimuthal anisotropy of charged particles produced in*
 843 *$\sqrt{s_{NN}} = 5.02$ TeV Pb+Pb collisions with the ATLAS detector*, *Eur. Phys. J.* **C78** (2018) 997, arXiv:
 844 [1808.03951 \[nucl-ex\]](#) (cit. on p. 6).
- 845 [61] PHENIX Collaboration, *Elliptic Flow of Identified Hadrons in Au + Au Collisions at $\sqrt{s_{NN}} = 200$*
 846 *GeV*, *Phys. Rev. Lett.* **91** (18 2003) 182301 (cit. on p. 6).
- 847 [62] CMS Collaboration, *Non-Gaussian elliptic-flow fluctuations in PbPb collisions at $\sqrt{s_{NN}} = 5.02$ TeV*,
 848 *Phys. Lett.* **B789** (2019) 643, arXiv: [1711.05594 \[nucl-ex\]](#) (cit. on p. 6).

- 849 [63] ALICE Collaboration, *Anisotropic Flow of Charged Particles in Pb-Pb Collisions at $\sqrt{s_{NN}} = 5.02$*
 850 *TeV*, *Phys. Rev. Lett.* **116** (13 2016) 132302 (cit. on p. 6).
- 851 [64] M. Connors, C. Nattrass, R. Reed and S. Salur, *Jet measurements in heavy ion physics*, *Rev. Mod.*
 852 *Phys.* **90** (2 2018) 025005 (cit. on p. 6).
- 853 [65] A. M. Poskanzer and S. A. Voloshin, *Methods for analyzing anisotropic flow in relativistic nuclear*
 854 *collisions*, *Phys. Rev.* **C58** (1998) 1671, arXiv: [nucl-ex/9805001 \[nucl-ex\]](#) (cit. on p. 6).
- 855 [66] S. A. Voloshin, A. M. Poskanzer and R. Snellings, *Collective phenomena in non-central nuclear*
 856 *collisions*, *Landolt-Bornstein* **23** (2010) 293, arXiv: [0809.2949 \[nucl-ex\]](#) (cit. on pp. 6, 7).
- 857 [67] D. Teaney, J. Lauret and E. V. Shuryak, *A Hydrodynamic description of heavy ion collisions at the*
 858 *SPS and RHIC*, (2001), arXiv: [nucl-th/0110037 \[nucl-th\]](#) (cit. on p. 6).
- 859 [68] T. Hirano, U. Heinz, D. Kharzeev, R. Lacey and Y. Nara, *Hadronic dissipative effects on elliptic*
 860 *flow in ultrarelativistic heavy-ion collisions*, *Physics Letters B* **636** (2006) 299 , ISSN: 0370-2693, URL:
 861 <http://www.sciencedirect.com/science/article/pii/S0370269306003996> (cit. on p. 6).
- 862 [69] ALICE Collaboration, *Higher harmonic anisotropic flow measurements of charged particles in Pb-Pb*
 863 *collisions at $\sqrt{s_{NN}}=2.76$ TeV*, *Phys. Rev. Lett.* **107** (2011) 032301, arXiv: [1105.3865 \[nucl-ex\]](#)
 864 (cit. on pp. 6, 7).
- 865 [70] H. Niemi, K. J. Eskola and R. Paatelainen, *Event-by-event fluctuations in a perturbative QCD*
 866 *+ saturation + hydrodynamics model: Determining QCD matter shear viscosity in ultrarelativistic*
 867 *heavy-ion collisions*, *Phys. Rev.* **C93** (2016) 024907, arXiv: [1505.02677 \[hep-ph\]](#) (cit. on pp. 6, 7).
- 868 [71] BRAHMS Collaboration, *Quark-gluon plasma and color glass condensate at RHIC? The perspective*
 869 *from the BRAHMS experiment*, *Nuclear Physics A* **757** (2005) 1 , First Three Years of Opera-
 870 tion of RHIC, ISSN: 0375-9474, URL: <http://www.sciencedirect.com/science/article/pii/S0375947405002770> (cit. on p. 8).
- 872 [72] M. Gyulassy and L. McLerran, *New forms of QCD matter discovered at RHIC*, *Nuclear Physics A*
 873 **750** (2005) 30 , Quark-Gluon Plasma. New Discoveries at RHIC: Case for the Strongly Interacting
 874 Quark-Gluon Plasma. Contributions from the RBRC Workshop held May 14-15, 2004, ISSN: 0375-9474,
 875 URL: <http://www.sciencedirect.com/science/article/pii/S0375947404011480> (cit. on p. 8).
- 876 [73] PHENIX Collaboration, *Transverse energy production and charged-particle multiplicity at midrapidity*
 877 *in various systems from $\sqrt{s_{NN}} = 7.7$ to 200 GeV*, *Phys. Rev. C* **93** (2 2016) 024901, URL: <https://link.aps.org/doi/10.1103/PhysRevC.93.024901> (cit. on p. 8).

- [74] ALICE Collaboration, *Measurement of transverse energy at midrapidity in Pb-Pb collisions at $\sqrt{s_{NN}} = 2.76 \text{ TeV}$* , *Phys. Rev. C* **94** (3 2016) 034903, URL: <https://link.aps.org/doi/10.1103/PhysRevC.94.034903> (cit. on p. 8).
- [75] CMS Collaboration, *Measurement of the Pseudorapidity and Centrality Dependence of the Transverse Energy Density in Pb-Pb Collisions at $\sqrt{s_{NN}} = 2.76 \text{ TeV}$* , *Phys. Rev. Lett.* **109** (15 2012) 152303, URL: <https://link.aps.org/doi/10.1103/PhysRevLett.109.152303> (cit. on p. 8).
- [76] F. Karsch, ‘Lattice QCD at High Temperature and Density’, *Lectures on Quark Matter*, ed. by W. Plessas and L. Mathelitsch, Springer Berlin Heidelberg, 2002 209, ISBN: 978-3-540-45792-3, URL: https://doi.org/10.1007/3-540-45792-5_6 (cit. on p. 8).
- [77] A. Bazavov et al., *Equation of state in (2 + 1)-flavor QCD*, *Phys. Rev. D* **90** (9 2014) 094503, URL: <https://link.aps.org/doi/10.1103/PhysRevD.90.094503> (cit. on p. 8).
- [78] R. Glauber, *Lectures in theoretical physics*, ed. WE Brittin and LG Dunham, Interscience, New York **1** (1959) 315 (cit. on p. 9).
- [79] R. Glauber et al., *Lectures in theoretical physics*, 1959 (cit. on p. 9).
- [80] H. D. Vries, C. D. Jager and C. D. Vries, *Nuclear charge-density-distribution parameters from elastic electron scattering*, *Atomic Data and Nuclear Data Tables* **36** (1987) 495 , ISSN: 0092-640X (cit. on pp. 9, 10).
- [81] M. L. Miller, K. Reygers, S. J. Sanders and P. Steinberg, *Glauber Modeling in High-Energy Nuclear Collisions*, *Annual Review of Nuclear and Particle Science* **57** (2007) 205 (cit. on pp. 9, 10, 12, 24).
- [82] B. Alver, M. Baker, C. Loizides and P. Steinberg, *The PHOBOS Glauber Monte Carlo*, (2008), arXiv: [0805.4411 \[nucl-ex\]](https://arxiv.org/abs/0805.4411) (cit. on p. 9).
- [83] D. Kharzeev and M. Nardi, *Hadron production in nuclear collisions at RHIC and high density QCD*, *Phys. Lett. B* **507** (2001) 121, arXiv: [nucl-th/0012025 \[nucl-th\]](https://arxiv.org/abs/hep-ph/0012025) (cit. on p. 11).
- [84] A. Bialas, M. Bleszynski and W. Czyz, *Multiplicity Distributions in Nucleus-Nucleus Collisions at High-Energies*, *Nucl. Phys.* **B111** (1976) 461 (cit. on p. 11).
- [85] ATLAS Collaboration, *Centrality determination in $\sqrt{s_{NN}} = 5.02 \text{ TeV}$ Pb+Pb collision data in 2015*, tech. rep. ATL-COM-PHYS-2016-1287, CERN, 2016 (cit. on p. 12).
- [86] G. S. Bali, H. Neff, T. Düssel, T. Lippert and K. Schilling, *Observation of string breaking in QCD*, *Phys. Rev. D* **71** (11 2005) 114513, URL: <https://link.aps.org/doi/10.1103/PhysRevD.71.114513> (cit. on p. 12).

- 909 [87] O. Collaboration, *Experimental properties of gluon and quark jets from a point source*, *Eur. Phys. J. C*
 910 **11** (1999) 217, arXiv: [hep-ex/9903027 \[hep-ex\]](#) (cit. on p. 12).
- 911 [88] SLAC-LBL Collaboration, *Evidence for Jet Structure in Hadron Production by e^+e^- Annihilation*,
 912 *Phys. Rev. Lett.* **35** (1975) 1609 (cit. on p. 13).
- 913 [89] SLAC-LBL Collaboration, *Hadron Production by e^+e^- Annihilation at Center-of-mass Energies*
 914 *Between 2.6 GeV and 7.8 GeV*, *Phys. Rev. D* **26** (1982) 991 (cit. on p. 13).
- 915 [90] PLUTO Collaboration, *Jet Analysis of the $\Upsilon(9.46)$ Decay Into Charged Hadrons*, *Phys. Lett.* **82B**
 916 (1979) 449 (cit. on p. 13).
- 917 [91] PLUTO Collaboration, *Evidence for Gluon Bremsstrahlung in $e^+ e^-$ Annihilations at High-Energies*,
 918 *Phys. Lett. B* **86** (1979) 418 (cit. on p. 13).
- 919 [92] A. H. Mueller, *Jets at LEP and HERA*, *Journal of Physics G: Nuclear and Particle Physics* **17**
 920 (1991) 1443, URL: <https://doi.org/10.1088%2F0954-3899%2F17%2F10%2F001> (cit. on p. 13).
- 921 [93] G. Kramer and B. Lampe, *Jet Cross-Sections in $e^+ e^-$ Annihilation*, *Fortsch. Phys.* **37** (1989) 161
 922 (cit. on p. 13).
- 923 [94] T. Sjostrand, S. Mrenna and P. Z. Skands, *A Brief Introduction to PYTHIA 8.1*, *Comput. Phys.*
 924 *Commun.* **178** (2008) 852, arXiv: [0710.3820 \[hep-ph\]](#) (cit. on p. 13).
- 925 [95] G.-Y. Qin and X.-N. Wang, *Jet quenching in high-energy heavy-ion collisions*, *Int. J. Mod. Phys. E* **24**
 926 (2015) 1530014, arXiv: [1511.00790 \[hep-ph\]](#), URL: <https://doi.org/10.1142/S0218301315300143>
 927 (cit. on pp. 13, 14, 17).
- 928 [96] A. D. Martin, W. J. Stirling, R. S. Thorne and G. Watt, *Parton distributions for the LHC*, *The European*
 929 *Physical Journal C* **63** (2009) 189, ISSN: 1434-6052, URL: <https://doi.org/10.1140/epjc/s10052-009-1072-5> (cit. on p. 15).
- 931 [97] A. Majumder and M. Van Leeuwen, *The Theory and Phenomenology of Perturbative QCD Based Jet*
 932 *Quenching*, *Prog. Part. Nucl. Phys.* **66** (2011) 41, arXiv: [1002.2206 \[hep-ph\]](#) (cit. on pp. 14, 36).
- 933 [98] K. Olive, *Review of Particle Physics*, *Chinese Physics C* **40** (2016) 100001, URL: <https://doi.org/10.1088%2F1674-1137%2F40%2F10%2F100001> (cit. on p. 15).
- 935 [99] D. Britzger, K. Rabbertz, D. Savoiu, G. Sieber and M. Wobisch, *Determination of the strong coupling*
 936 *constant using inclusive jet cross section data from multiple experiments*, *Eur. Phys. J. C* **79** (2019) 68,
 937 arXiv: [1712.00480 \[hep-ph\]](#) (cit. on p. 15).

- 938 [100] M. Hirai, S. Kumano and T.-H. Nagai, *Determination of nuclear parton distribution functions and*
 939 *their uncertainties at next-to-leading order*, Phys. Rev. C **76** (6 2007) 065207 (cit. on p. 16).
- 940 [101] D. de Florian and R. Sassot, *Nuclear parton distributions at next to leading order*, Phys. Rev. D **69** (7
 941 2004) 074028 (cit. on p. 16).
- 942 [102] K. Eskola, H Paukkunen and C. Salgado, *EPS09 — A new generation of NLO and LO nuclear parton*
 943 *distribution functions*, Journal of High Energy Physics **2009** (2009) 065 (cit. on p. 16).
- 944 [103] S. J. Brodsky and H. J. Lu, *Shadowing and antishadowing of nuclear structure functions*, Phys. Rev.
 945 Lett. **64** (12 1990) 1342 (cit. on p. 16).
- 946 [104] European Muon Collaboration, *The ratio of the nucleon structure functions F2N for iron and deuterium*,
 947 Physics Letters B **123** (1983) 275 , ISSN: 0370-2693 (cit. on p. 16).
- 948 [105] O. Hen, E. Piasetzky and L. B. Weinstein, *New data strengthen the connection between short range*
 949 *correlations and the EMC effect*, Phys. Rev. C **85** (4 2012) 047301 (cit. on p. 16).
- 950 [106] K. Saito and T. Uchiyama, *Effect of the Fermi Motion on Nuclear Structure Functions and the Emc*
 951 *Effect*, Z. Phys. **A322** (1985) 299 (cit. on p. 16).
- 952 [107] CMS Collaboration, *Jet momentum dependence of jet quenching in PbPb collisions at sNN=2.76 TeV*,
 953 Physics Letters B **712** (2012) 176 , ISSN: 0370-2693 (cit. on p. 16).
- 954 [108] ATLAS collaboration, *Study of inclusive jet yields in Pb+Pb collisions at $\sqrt{s_{NN}} = 5.02$ TeV*, (2017)
 955 (cit. on p. 16).
- 956 [109] The CMS collaboration, *Measurement of transverse momentum relative to dijet systems in PbPb and*
 957 *pp collisions at $\sqrt{s_{NN}} = 2.76$ TeV*, Journal of High Energy Physics **2016** (2016) 6, ISSN: 1029-8479,
 958 URL: [https://doi.org/10.1007/JHEP01\(2016\)006](https://doi.org/10.1007/JHEP01(2016)006) (cit. on p. 16).
- 959 [110] S. Chatrchyan et al., *Jet momentum dependence of jet quenching in PbPb collisions at $\sqrt{s_{NN}} = 2.76$*
 960 *TeV*, Phys. Lett. **B712** (2012) 176, arXiv: [1202.5022 \[nucl-ex\]](https://arxiv.org/abs/1202.5022) (cit. on p. 17).
- 961 [111] R. Baier, Y. Dokshitzer, A. Mueller, S. Peigné and D. Schiff, *Radiative energy loss of high energy*
 962 *quarks and gluons in a finite-volume quark-gluon plasma*, Nuclear Physics B **483** (1997) 291 , ISSN:
 963 0550-3213 (cit. on p. 17).
- 964 [112] M. Gyulassy, P. Levai and I. Vitev, *Jet quenching in thin quark gluon plasmas. 1. Formalism*, Nucl.
 965 Phys. **B571** (2000) 197, arXiv: [hep-ph/9907461 \[hep-ph\]](https://arxiv.org/abs/hep-ph/9907461) (cit. on p. 17).
- 966 [113] U. A. Wiedemann, *Gluon radiation off hard quarks in a nuclear environment: Opacity expansion*, Nucl.
 967 Phys. **B588** (2000) 303, arXiv: [hep-ph/0005129 \[hep-ph\]](https://arxiv.org/abs/hep-ph/0005129) (cit. on p. 17).

- 968 [114] P. B. Arnold, G. D. Moore and L. G. Yaffe, *Photon emission from ultrarelativistic plasmas*, **JHEP** **11**
 969 (2001) 057, arXiv: [hep-ph/0109064 \[hep-ph\]](#) (cit. on p. 17).
- 970 [115] X.-F. Guo and X.-N. Wang, *Multiple scattering, parton energy loss and modified fragmentation*
 971 *functions in deeply inelastic e A scattering*, **Phys. Rev. Lett.** **85** (2000) 3591, arXiv: [hep-ph/0005044](#)
 972 [\[hep-ph\]](#) (cit. on p. 17).
- 973 [116] R. Atkin, *Review of jet reconstruction algorithms*, **Journal of Physics: Conference Series** **645** (2015) 012008,
 974 URL: [https://doi.org/10.1088%2F1742-6596%2F645%2F1%2F012008](https://doi.org/10.1088/2F1742-6596%2F645%2F1%2F012008) (cit. on p. 18).
- 975 [117] UA1 Collaboration, *Hadronic jet production at the CERN proton-antiproton collider*, **Physics Letters**
 976 **B** **132** (1983) 214 , ISSN: 0370-2693, URL: <http://www.sciencedirect.com/science/article/pii/037026938390254X> (cit. on p. 18).
- 978 [118] G. C. Blazey et al., ‘Run II jet physics’, *QCD and weak boson physics in Run II. Proceedings, Batavia,*
 979 *USA, March 4-6, June 3-4, November 4-6, 1999*, 2000 47, arXiv: [hep-ex/0005012 \[hep-ex\]](#), URL:
 980 http://lss.fnal.gov/cgi-bin/find_paper.pl?conf=00-092 (cit. on p. 18).
- 981 [119] G. P. Salam and G. Soyez, *A practical seedless infrared-safe cone jet algorithm*, **Journal of High Energy**
 982 **Physics** **2007** (2007) 086 (cit. on pp. 18, 19).
- 983 [120] S. Catani, Y. L. Dokshitzer, M. H. Seymour and B. R. Webber, *Longitudinally invariant K_t clustering*
 984 *algorithms for hadron hadron collisions*, **Nucl. Phys.** **B406** (1993) 187 (cit. on p. 18).
- 985 [121] M. Cacciari, G. P. Salam and G. Soyez, *The Anti- $k(t)$ jet clustering algorithm*, **JHEP** **0804** (2008) 063,
 986 arXiv: [0802.1189 \[hep-ph\]](#) (cit. on pp. 18, 20).
- 987 [122] Y. L. Dokshitzer, G. D. Leder, S. Moretti and B. R. Webber, *Better jet clustering algorithms*, **JHEP**
 988 **08** (1997) 001, arXiv: [hep-ph/9707323 \[hep-ph\]](#) (cit. on p. 18).
- 989 [123] G. P. Salam, *Towards Jetography*, **Eur. Phys. J.** **C67** (2010) 637, arXiv: [0906.1833 \[hep-ph\]](#) (cit. on
 990 p. 18).
- 991 [124] ATLAS Collaboration, *Measurement of the jet radius and transverse momentum dependence of*
 992 *inclusive jet suppression in lead-lead collisions at $\sqrt{s_{NN}} = 2.76 \text{ TeV}$ with the ATLAS detector*, **Phys.**
 993 **Lett.** **B719** (2013) 220, arXiv: [1208.1967 \[hep-ex\]](#) (cit. on pp. 38, 48).
- 994 [125] PHENIX Collaboration, *Suppression of Hadrons with Large Transverse Momentum in Central Au+Au*
 995 *Collisions at $\sqrt{s_{NN}} = 130\text{GeV}$* , **Phys. Rev. Lett.** **88** (2 2001) 022301, URL: <https://link.aps.org/doi/10.1103/PhysRevLett.88.022301> (cit. on pp. 21, 22).

- 997 [126] ISR Collaboration, *Large transverse momentum π^0 production in $\alpha\alpha$, dd and pp collisions at the*
 998 *CERN ISR*, Physics Letters B **185** (1987) 213 , ISSN: 0370-2693, URL: <http://www.sciencedirect.com/science/article/pii/0370269387915577> (cit. on p. 22).
- 1000 [127] E. Wang and X.-N. Wang, *Interplay of soft and hard processes and hadron p_T spectra in pA and AA*
 1001 *collisions*, Phys. Rev. C **64** (3 2001) 034901, URL: <https://link.aps.org/doi/10.1103/PhysRevC.64.034901> (cit. on p. 22).
- 1003 [128] PHENIX Collaboration, *Measurement of Direct Photons in Au+Au Collisions at $\sqrt{s_{NN}} = 200$ GeV*,
 1004 Phys. Rev. Lett. **109** (15 2012) 152302, URL: <https://link.aps.org/doi/10.1103/PhysRevLett.109.152302> (cit. on p. 22).
- 1006 [129] D. Antreasyan et al., *Production of hadrons at large transverse momentum in 200, 300, and 400 GeV*
 1007 *pp and p-nucleus collisions*, Phys. Rev. D **19** (3 1979) 764, URL: <https://link.aps.org/doi/10.1103/PhysRevD.19.764> (cit. on p. 21).
- 1009 [130] ATLAS Collaboration, *Measurement of jet p_T correlations in Pb+Pb and pp collisions at $\sqrt{s_{NN}} = 2.76$*
 1010 *TeV with the ATLAS detector*, Phys. Lett. **B774** (2017) 379, arXiv: [1706.09363 \[hep-ex\]](https://arxiv.org/abs/1706.09363) (cit. on
 1011 pp. 22, 23, 25).
- 1012 [131] R. Reed, *Full Jet Reconstruction in 2.76 TeV pp and Pb-Pb collisions in the ALICE experiment*,
 1013 Journal of Physics: Conference Series **446** (2013) 012006, URL: <https://doi.org/10.1088/2F1742-6596%2F446%2F1%2F012006> (cit. on pp. 23, 24).
- 1015 [132] ATLAS Collaboration, *Measurements of the Nuclear Modification Factor for Jets in Pb+Pb Collisions*
 1016 *at $\sqrt{s_{NN}} = 2.76$ TeV with the ATLAS Detector*, Phys. Rev. Lett. **114** (2015) 072302, arXiv: [1411.2357 \[hep-ex\]](https://arxiv.org/abs/1411.2357) (cit. on pp. 24, 25, 32, 33).
- 1018 [133] ATLAS Collaboration, *Measurement of the nuclear modification factor for inclusive jets in Pb+Pb*
 1019 *collisions at $\sqrt{s_{NN}} = 5.02$ TeV with the ATLAS detector*, Phys. Lett. **B790** (2019) 108, arXiv:
 1020 [1805.05635 \[nucl-ex\]](https://arxiv.org/abs/1805.05635) (cit. on pp. 24, 25).
- 1021 [134] CMS Collaboration, *Measurement of inclusive jet cross sections in pp and PbPb collisions at $\sqrt{s_{NN}} =$*
 1022 *2.76 TeV*, Phys. Rev. C **96** (2017) 015202, arXiv: [1609.05383 \[nucl-ex\]](https://arxiv.org/abs/1609.05383) (cit. on pp. 24, 25, 33, 35,
 1023 38).
- 1024 [135] ATLAS Collaboration, *Measurement of jet fragmentation in Pb+Pb and pp collisions at $\sqrt{s_{NN}} = 5.02$*
 1025 *TeV with the ATLAS detector*, Phys. Rev. **C98** (2018) 024908, arXiv: [1805.05424 \[nucl-ex\]](https://arxiv.org/abs/1805.05424) (cit. on
 1026 pp. 25–28).

- 1027 [136] ALICE Collaboration, *Measurement of jet suppression in central Pb–Pb collisions at $\sqrt{s_{NN}} = 2.76$ TeV*,
 1028 Physics Letters B **746** (2015) 1 , ISSN: 0370-2693, URL: <http://www.sciencedirect.com/science/article/pii/S0370269315002828> (cit. on p. 25).
- 1029
 1030 [137] CMS Collaboration, *Observation and studies of jet quenching in PbPb collisions at nucleon-nucleon*
 1031 *center-of-mass energy = 2.76 TeV*, Phys. Rev. **C84** (2011) 024906, arXiv: [1102.1957 \[nucl-ex\]](https://arxiv.org/abs/1102.1957)
 1032 (cit. on pp. 25, 30).
- 1033 [138] STAR Collaboration, *Dijet imbalance measurements in Au+Au and pp collisions at $\sqrt{s_{NN}} = 200$*
 1034 *GeV at STAR*, Phys. Rev. Lett. **119** (6 2017) 062301, URL: <https://link.aps.org/doi/10.1103/PhysRevLett.119.062301> (cit. on p. 25).
- 1035
 1036 [139] M. Spousta and B. Cole, *Interpreting single jet measurements in Pb + Pb collisions at the LHC*, Eur.
 1037 Phys. J. C **76** (2016) 50, arXiv: [1504.05169 \[hep-ph\]](https://arxiv.org/abs/1504.05169) (cit. on pp. 27, 30–32, 39).
- 1038 [140] Y.-T. Chien et al., *Jet Quenching from QCD Evolution*, Phys. Rev. **D93** (2016) 074030, arXiv:
 1039 [1509.02936 \[hep-ph\]](https://arxiv.org/abs/1509.02936) (cit. on p. 27).
- 1040 [141] Z.-B. Kang et al., *Inclusive production of small radius jets in heavy-ion collisions*, Phys. Lett. **B769**
 1041 (2017) 242, arXiv: [1701.05839 \[hep-ph\]](https://arxiv.org/abs/1701.05839) (cit. on p. 27).
- 1042 [142] J. Casalderrey-Solana et al., *A Hybrid Strong/Weak Coupling Approach to Jet Quenching*, JHEP **10**
 1043 (2014) 019, arXiv: [1405.3864 \[hep-ph\]](https://arxiv.org/abs/1405.3864) (cit. on pp. 27, 36).
- 1044 [143] A. M. Sirunyan et al., *Jet properties in PbPb and pp collisions at $\sqrt{s_{NN}} = 5.02$ TeV*, JHEP **05**
 1045 (2018) 006, arXiv: [1803.00042 \[nucl-ex\]](https://arxiv.org/abs/1803.00042) (cit. on pp. 27, 29).
- 1046 [144] J.-P. Blaizot, E. Iancu and Y. Mehtar-Tani, *Medium-induced QCD cascade: democratic branching and*
 1047 *wave turbulence*, Phys. Rev. Lett. **111** (2013) 052001, arXiv: [1301.6102 \[hep-ph\]](https://arxiv.org/abs/1301.6102) (cit. on p. 30).
- 1048 [145] J. Casalderrey-Solana, Y. Mehtar-Tani, C. A. Salgado and K. Tywoniuk, *New picture of jet quenching*
 1049 *dictated by color coherence*, Phys. Lett. **B725** (2013) 357, arXiv: [1210.7765 \[hep-ph\]](https://arxiv.org/abs/1210.7765) (cit. on p. 30).
- 1050 [146] R. Baier, Y. L. Dokshitzer, A. H. Mueller and D. Schiff, *Quenching of hadron spectra in media*, JHEP
 1051 **09** (2001) 033, arXiv: [hep-ph/0106347 \[hep-ph\]](https://arxiv.org/abs/hep-ph/0106347) (cit. on p. 31).
- 1052 [147] ATLAS Collaboration, *Measurement of inclusive jet charged-particle fragmentation functions in*
 1053 *Pb+Pb collisions at $\sqrt{s_{NN}} = 2.76$ TeV with the ATLAS detector*, Phys. Lett. B **739** (2014) 320, arXiv:
 1054 [1406.2979 \[hep-ex\] \[hep-ex\]](https://arxiv.org/abs/1406.2979) (cit. on p. 32).
- 1055 [148] Y. Tachibana, N.-B. Chang and G.-Y. Qin, *Full jet in quark-gluon plasma with hydrodynamic medium*
 1056 *response*, Phys. Rev. **C95** (2017) 044909, arXiv: [1701.07951 \[nucl-th\]](https://arxiv.org/abs/1701.07951) (cit. on pp. 33–36).

- 1057 [149] ALICE Collaboration, *Measurement of charged jet suppression in Pb-Pb collisions at $\sqrt{s_{NN}} = 2.76$ TeV*, JHEP **03** (2014) 013, arXiv: [1311.0633 \[nucl-ex\]](#) (cit. on pp. 33, 38).
- 1058
1059 [150] CMS Collaboration, *Modification of jet shapes in PbPb collisions at $\sqrt{s_{NN}} = 2.76$ TeV*, Phys. Lett. B**730** (2014) 243, arXiv: [1310.0878 \[nucl-ex\]](#) [nucl-ex] (cit. on pp. 36, 39).
- 1060
1061 [151] Z. Hulcher et al., *Resolution Effects in the Hybrid Strong/Weak Coupling Model*, (2017), arXiv: [1707.05245 \[hep-ph\]](#) (cit. on pp. 36–39).
- 1062
1063 [152] J. Casalderrey-Solana et al., *Angular Structure of Jet Quenching Within a Hybrid Strong/Weak Coupling Model*, JHEP **03** (2017) 135, arXiv: [1609.05842 \[hep-ph\]](#) (cit. on pp. 36, 37).
- 1064
1065 [153] P. M. Chesler and K. Rajagopal, *On the Evolution of Jet Energy and Opening Angle in Strongly Coupled Plasma*, JHEP **05** (2016) 098, arXiv: [1511.07567 \[hep-th\]](#) (cit. on p. 36).
- 1066
1067 [154] P. M. Chesler and K. Rajagopal, *Jet quenching in strongly coupled plasma*, Phys. Rev. D**90** (2014) 025033, arXiv: [1402.6756 \[hep-th\]](#) (cit. on p. 36).
- 1068
1069 [155] P. Jacobs and X.-N. Wang, *Matter in extremis: Ultrarelativistic nuclear collisions at RHIC*, Prog. Part. Nucl. Phys. **54** (2005) 443, arXiv: [hep-ph/0405125 \[hep-ph\]](#) (cit. on p. 36).
- 1070
1071 [156] J. Casalderrey-Solana, H. Liu, D. Mateos, K. Rajagopal and U. A. Wiedemann, *Gauge/String Duality, Hot QCD and Heavy Ion Collisions*, (2011), arXiv: [1101.0618 \[hep-th\]](#) (cit. on p. 36).
- 1072
1073 [157] J. Casalderrey-Solana, J. G. Milhano and P. Quiroga-Arias, *Out of Medium Fragmentation from Long-Lived Jet Showers*, Phys. Lett. B**710** (2012) 175, arXiv: [1111.0310 \[hep-ph\]](#) (cit. on p. 36).
- 1074
1075 [158] T. Hirano, P. Huovinen and Y. Nara, *Elliptic flow in Pb+Pb collisions at $\sqrt{s_{NN}} = 2.76$ TeV: hybrid model assessment of the first data*, Phys. Rev. C**84** (2011) 011901, arXiv: [1012.3955 \[nucl-th\]](#) (cit. on p. 37).
- 1076
1077 [159] J. Rusnak, *Inclusive spectrum of charged jets in central Au+Au collisions at $\sqrt{s_{NN}} = 200$ GeV by STAR*, PoS EPS-HEP**2013** (2013) 191 (cit. on p. 38).
- 1078
1079 [160] CMS Collaboration, *Measurement of jet fragmentation in PbPb and pp collisions at $\sqrt{s_{NN}} = 2.76$ TeV*, Phys. Rev. C **90** (2014) 024908, arXiv: [1406.0932 \[nucl-ex\]](#) [nucl-ex] (cit. on p. 39).
- 1080
1081 [161] L. Evans and P. Bryant, *LHC Machine*, Journal of Instrumentation **3** (2008) S08001 (cit. on p. 41).
- 1082
1083 [162] C. Lefevre, ‘The CERN accelerator complex’, 2008 (cit. on p. 42).
- 1084
1085 [163] ATLAS Collaboration, *The ATLAS Experiment at the CERN Large Hadron Collider*, JINST **3** (2008) S08003 (cit. on pp. 44, 45, 47).

- 1086 [164] A. La Rosa, *The ATLAS Insertable B-Layer: from construction to operation*, JINST **11** (2016) C12036,
1087 arXiv: [1610.01994 \[physics.ins-det\]](https://arxiv.org/abs/1610.01994) (cit. on p. 44).
- 1088 [165] ATLAS Collaboration, *ATLAS Insertable B-Layer Technical Design Report*, tech. rep., 2010 (cit. on
1089 p. 44).
- 1090 [166] K. Potamianos, *The upgraded Pixel detector and the commissioning of the Inner Detector tracking of*
1091 *the ATLAS experiment for Run-2 at the Large Hadron Collider*, tech. rep. ATL-PHYS-PROC-2016-104,
1092 15 pages, EPS-HEP 2015 Proceedings: CERN, 2016, URL: <https://cds.cern.ch/record/2209070>
1093 (cit. on p. 45).